Modified Hematite Photoelectrodes for Solar Energy Conversion

Haowei Huang

Master by Research

University of York

Chemistry

Dec 2016

Abstract

Photoelectrochemical water splitting has been considered as an attractive way to transform solar into chemical energy, since photoelectrochemistry of TiO_2 was reported in 1972. Hematite (Fe_2O_3) is a promising material to achieve a higher efficiency because of a smaller band gap, and because it is stable, non-toxic and cheap. However, because (1) low mobility of carriers (~0.1 $cm^2 V^{-1}s^{-1}$), (2) short hole diffusion lengths, (3) low rate of water oxidation (poor catalysis), (4) high electron-hole recombination rates and (5) inhibited hydrogen evolution due to the conduction band energetics, the reported efficiencies of Fe_2O_3 are notoriously lower than the theoretically limiting value. Many strategies to address these problems have been developed. Nanostructuring, doping, heterojunctions and surface modification have been used to lower the onset potential, improve the light absorption, charge transport and reduce recombination.

Herein is described the synthesis of two kinds of morphology of Fe_2O_3 by hydrothermal methods. Doping, homojunctions,and surface modification were attempted to enhance the efficiency of Fe_2O_3 for photoelectrochemial water oxidation. The impact of these modifications has been analysed by structural, spectroscopic and photoelectrochemical methods. Specifically, a new layered Co-doped Fe_2O_3/Sn-doped Fe_2O_3/FTO substrate (Co/Sn/Fe_2O_3) n-n homojunction photoanode was synthesized, CdS and Cu_2O nanoparticles were loaded on the surface of Fe_2O_3 nanorods by a chemical bath method and amorphous CoOx as water oxidation catalyst was loaded on the surface of Fe_2O_3 nanorod arrays.

Table of Contents

Table of Figures

Table of Tables

List of Accompanying Material

A digital copy of this thesis is included on a CD in the back of this volume.

Acknowledgements

There are many people I wish to thank for their support and help.

First, I would like to thank my supervisor Richard Douthwaite for his academic support and guidance. Thanks for his help for the application of PhD position in KU Leuven. I am grateful to my IPM Victor Chechik, for the useful discussions and advice in TAP meetings. I would like to thank Ian Wright and Adrian Whitwood who gave me lots of help in SEM and XRD. I would like to thank all staff in the department. I am also grateful to the Wild Fund Scholarship.

Around Richard's group, I would like to thank Menglong and Ruifei, firstly. They help me fit into the unfamiliar environment quickly and chatting with them is my softest time in the lab. Mina, he is always nice and friendly, I would like to thank him for sharing with interesting talks. Thank you, Ben, who is always kind to me. Thank you also to Chris, who helped me a lot on hydrothermal synthesis. I would like to thank all members in E014.

Lastly, I would like to thank my family. My wife Wei Wei always supports my studies and takes care of my son, Yicheng. I am extremely grateful for everything my parents have done for me.

Dec 2016

Declaration

The work presented in this thesis is to the best of my knowledge original. This work has not previously been presented for an award at this, or any other, University. All sources are acknowledged as References. The work contained within is entirely my own, with the following exception:

- The TEM and XPS were performed by PhD student Jinjin Ling in Fuzhou University in China.
- The Impendence tests in chapter 3 were performed by Master student Yingguang Zhang in Fuzhou University in China.

Chapter 1

Introduction

1.1: Overview

Solar energy has always been considered a major energy resource with significant capacity to solve energy and environmental problems.[1, 2, 3] The key factor to achieve large-scale use of solar energy is the conversion and storage of solar energy, which has low energy density, to chemical energy.[4] Artificial photosystems, including solar photovoltaic devices, photoelectrochemical cells and photocatalysis with electrons and protons derived from water, is a promising way to accomplish the conversion.[5, 6, 7, 8, 9, 10] Compared with photovoltaic devices and photocatalysis, photoelectrochemical cells could reach a higher efficiency as an external voltage can be applied.[11, 12] The aim of this work is to investigate the synthesis and properties of Fe_2O_3 photoanodes and to develop different methods to modify and improve the photoelectrochemical properties. This chapter will present a brief review of semiconductor photoelectrode, strategies to efficiency improvement and relevant photoelectrochemical behaviour.

1.2 Energy crisis

According to some publications, the consumption of fuels will reach approximately 25 TW (1TW = 10^{12}W) in the middle of this century.[13] However, since the 1st industrial revolution, fossil fuel acts as the main energy resource to support human society. Some greenhouse and toxic gases, like CO_2, SO_2, NO and so on, are byproducts of fossil fuel combustion. In the last few years, around 30Gt (1Gt = 10^9t) of CO_2 was released per year. Furthermore, fossil fuels are not renewable, and take thousands of years to produce. More and more people recognize that fossil fuels are a limited resource and are the source of greenhouse gases released during combustion. This results in global warming, one of the most severe problems of the 21st century. Alternative energy sources, such as solar, nuclear, wind and others, have therefore attracted great attention from all society.

Solar energy, as a safe, clean, abundant and sustainable source of energy presents a great opportunity. Approximately 120 thousand TW (1TW = 10^{12}W) of solar energy is received by earth and the worldwide energy consumption rate is around 15 TW.[11]

Currently there are three main methods to utilize solar energy: (1) solar energy is transferred to heat energy which is close to our daily life, such as solar water heaters; (2) the conversion between solar energy and electrical energy, such as a photovoltage in a solar cell (3) solar energy is converted to chemical energy, such as in photocatalysis or photoelectrochemistry.[14, 15, 16, 17, 18]

1.3: Semiconductor photocatalysis

Useful photocatalytic reactions for energy storage are “uphill”, involving a large positive change in the Gibbs free energy, therefore storing photon energy in chemical bonds.[11, 19]

Since Fujishima and Honda first reported the TiO_2 electrode for hydrogen production through photoelectrochemical water splitting under UV light in 1972, related photocatalysis has attracted more and more attention.[12] Materials with photocatalytic properties have been used to convert solar energy into chemical energy through reducing or oxidizing to acquire suitable products including hydrogen, carbon monoxide, hydrogen peroxide, and formic acid.[20, 21, 22]

Semiconductors exhibit a band energy structure consisting of the valence band which contains lots of trapped electrons in bonds, and empty conduction bands separated by a band gap between them. When the excitation energy is greater than the band gap, electrons are excited and move to the empty conduction band and the same amount of holes are generated in the valence band.

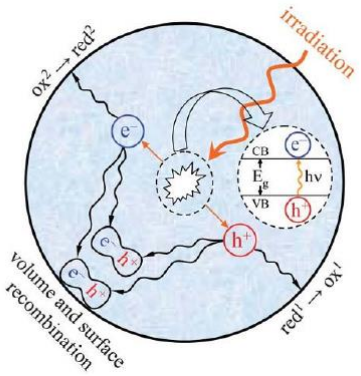

Figure 1: Representation of a semiconductor-photocatalyzed reaction.[23]

Figure 1 shows the basic physical process when a semiconductor photocatalyst is under light irradiation. To be more specific, the photocatalytic reaction consists of three processes: (i) absorption of photons, electrons and holes are generated in the conduction band and valence band, respectively; (ii) charge separation and migration to the surface reaction sites; (iii) on the surface reaction sites, the holes and electrons undergo oxidation and reduction reactions.[24, 25]

During this process, the photogenerated electrons and holes can recombine in the bulk and on the surface, which is the main reason limiting the activity of a photocatalyst. Reducing the recombination is a key factor to improve the photocatalytic efficiency and a lot of methods have been tried.[11] Lin and co-workers changed the nanostructure to minimize the distance carriers travel to decrease the recombination probability.[26] A junction structure can induce an inner field to accelerate the separation of photo-generated carriers.[27] Doping is also an efficient method to decrease recombination as the doping centre can lengthen the diffusion distance of charge carriers.[5, 28] Surface modification can also reduce recombination on the surface.[29]

1.4: Photocatalytic Water-Splitting

Splitting water into hydrogen and oxygen is a typical “uphill reaction”.[5] In traditional

electrolysis, water splitting to produce O_2 and H_2 requires a bias lager than 1.23 V, which requires energy consumption.

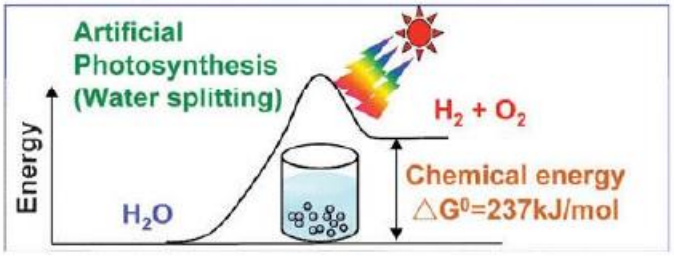

Figure 2: photocatalytic water splitting [30]

However, solar energy could be used to drive photocatalytic and PEC water splitting, as shown in Figure 2. Electrons and holes are generated inside the excited photocatalyst, transferred to surface active sites and subsequently consumed by surface redox reactions. The overall reactions are shown in Equation 1.[31]

Equation 1: $2H_2O \rightarrow 2H_2 + O_2$

The half reactions are described as follows:

$$2H^+ + 2e^- \rightarrow H_2$$

$$2H_2O + 4h^+ \rightarrow O_2 + 4H^+$$

Currently, scientists use two main kinds of photocatalytic system to achieve water splitting.[11] The first type of photocatalytic system is shown in Figure 3. This system uses a single photocatalyst with a band structure to satisfy the energy requirement of water splitting, like TiO_2, $SrTiO_3$ and other wide bandgap oxides. The position of the conduction band should be more negative than the redox reaction H^+/H_2, and the valence band should be at a more positive potential than the redox reaction O_2/H_2O.

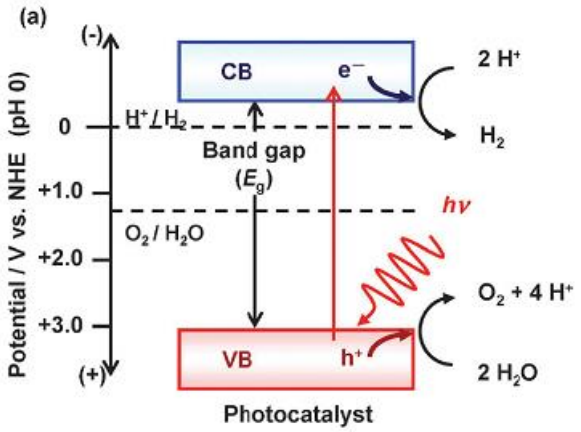

Figure 3: Energy diagrams of photocatalytic water splitting based on one-step excitation.[11]

An alternative, based on natural photosynthesis, is coupling two photocatalysts to achieve water splitting, as shown in Figure 4. In this scheme, it contains one O_2 evolution photocatalyst and one H_2 evolution photocatalyst. Compared with a single photocatalyst system, this system could enlarge the photo-response area and enhance the photo-generated carrier separation. This two-step photocatalytic system is commonly called the ‘‘Z-scheme’’.[32, 33]

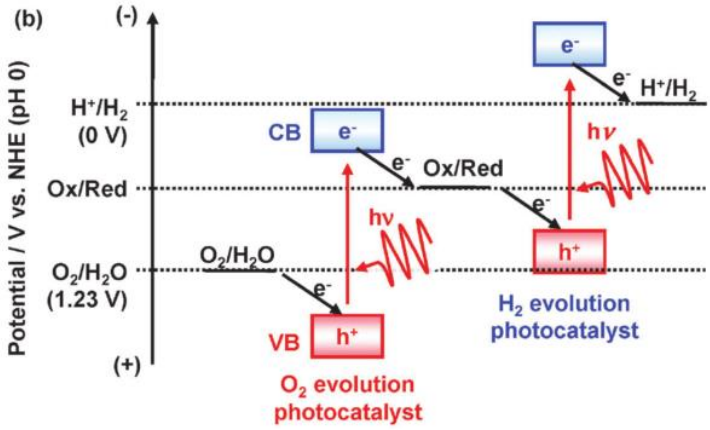

*Figure 4: “*Z-scheme*” photocatalytic system for water splitting.*[11]

1.5: Photoelectrochemical Water-Splitting

In 1972, Fujishima described photo-assisted electrochemical water splitting, as shown in Figure 5.

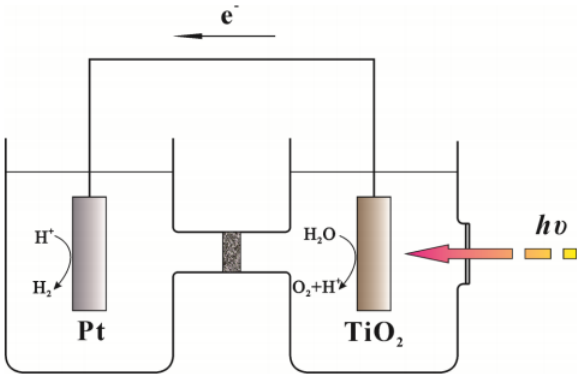

Figure 5: Scheme of photoelectrochemical cell in Fujishima and Honda's experiment.[12]

Rutile TiO_2 was illuminated by UV light whose energy is greater than the band gap energy of TiO_2, exciting electrons in the valence band to the conduction band. Under bias, the photo-generated electrons move to the Pt counter electrode and reduce protons from water to give H_2. The holes move to the surface of the TiO_2 and oxidize water to produce O_2 and release.protons. Since the discovery of the Honda–Fujishima system, photoelectrochemical (PEC) water splitting of semiconducting materials has been studied extensively, with the aim of producing systems that rely only on solar energy input and are cheap and stable.

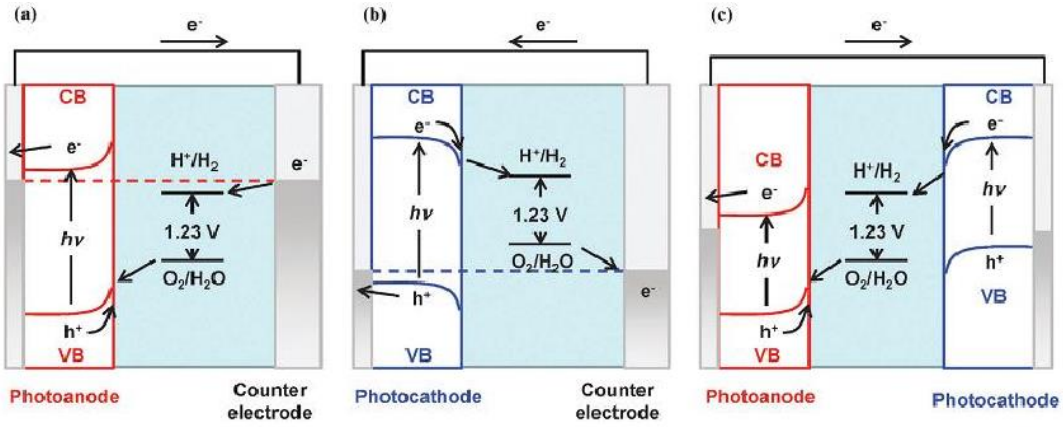

Figure 6: (a) Photoelectrochemical water splitting using one photoanode, (b) one photocathode and (c) photoanode and photocathode in tandem configuration.[11]

Figure 6 presents 3 kinds of PEC water splitting model. Figure 6a shows the system with semiconductor working as a photoanode and carbon or Pt as a cathode as for the original TiO_2 system of Fujishima and Honda. In Figure 6b, when the semiconductor is a photocathode, the photo-generated electrons move to the surface of the photocathode to reduce protons and release H_2 and the photo-generated holes are transferred to an anode. Alternatively the counter electrode can be replaced by a photoelectrode as shown in Figure 6c, giving two photoelectrodes, a photoanode connected to a photocathode.[11]

As the Fermi energy in a semiconductor and electrolyte solution are not at the same energy, the carriers will be transfered between surface and electrolyte solution causing band bending.[34] For photocathodes, p-type semiconductors produce band bending to higher potential whereas photoanode n-type semiconductors bend to lower potentials. n- and p-type semiconductors are used for photoanode and –cathode respectively to avoid corrosion and direct the majority carriers.

1.6: Photoanode material

In the last few decades, there is no doubt that TiO_2 is the most popular material based on its stability, nontoxicity and low cost. However, TiO_2, has a band gap of 3.2 eV in

the anatase crystalline phase, only absorbing UV light (wavelength λ < 387 nm) which limits the usage of solar light as the fraction of UV light is only 4% at the Earth's surface.[12] In addition, high charge recombination also limits its practical application. Although many improved works have been done, the quantum efficiency of TiO_2 is still lower than 10% under sun light irradiation. Therefore other materials which absorb more sun light and reduce recombination are a target. In addition modification strategies (doping, cocatalysts, morphology) have also been explored to improve known materials.

WO_3 is stable and a nontoxic material. The holes and electrons in WO_3 have a long diffusion length and importantly WO_3 is an indirect semiconductor with a 2.5-2.8 eV bandgap whose band edge absorption could reach 500 nm.[35, 36] Augustynski et al. demonstrated efficient water oxidation under visible light using a highly transparent nanoporous WO_3 photoelectrode.[35] Jingwei Huang and his co-workers combined WO_3 anode with an FeOOH OER catalyst to increase the photoactivity and the photostability.[37]

$BiVO_4$ is a semiconductor that is a well-known visible-light-responsive photocatalyst for water oxidation and was first reported by Kudo and coworkers as a photocatalyst for water oxidation.[38] However $BiVO_4$ suffers from poor electron transfer and collection in the photoelectrode.[39] Doping and addition of water oxidation cocatalysts have been used to improve the charge transport properties and reduce the surface recombination of the photogenerated carriers in $BiVO_4$.[40, 41, 42]

In 1978, Fe_2O_3 was first used for photocatalytic water splitting. Compared with TiO_2, with a narrow band gap (Eg = 2.1 eV) the absorption edge of Fe_2O_3 is around 560 nm. At the same time, Fe_2O_3 has advantages of low cost, abundance, nontoxicity and stability. Fe_2O_3 has therefore emerged as a promising material to achieve the high efficient conversion from solar energy to chemical energy and is the focus of this thesis.[43, 44]

1.7: Fe_2O_3 Photoanode

Hematite is an iron ore which is abundant in the Earth's crust. It is a low cost, non-toxic and stable material in aqueous solutions. Hematite Fe_2O_3 is the most thermodynamically stable and common crystal structure among all iron oxides. Hematite Fe_2O_3 is corundum-type structure and hexagonal with the lattice parameters a = 5.0356 Å, c = 13.7489 Å.[45] The crystal structure is shown in Figure 7.

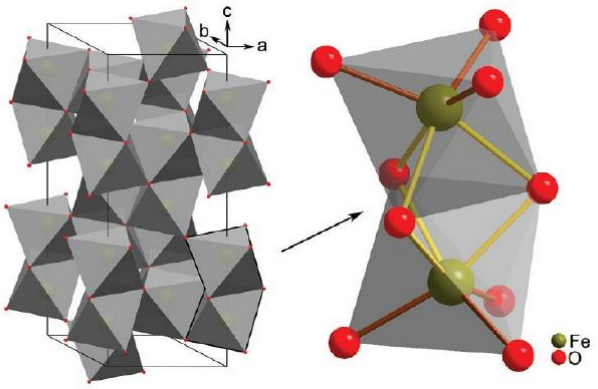

Figure 7: The unit cell and crystal structure of hematite[45]

Hematite Fe_2O_3 is an n-type semiconductor. As shown in Figure 8, the valence band (VB) position of Fe_2O_3 is positive enough to oxidize water, and is at +2.5 V vs RHE. However, a bias potential is required for proton reduction as the conduction band (CB) energy is too positive.[44, 45]

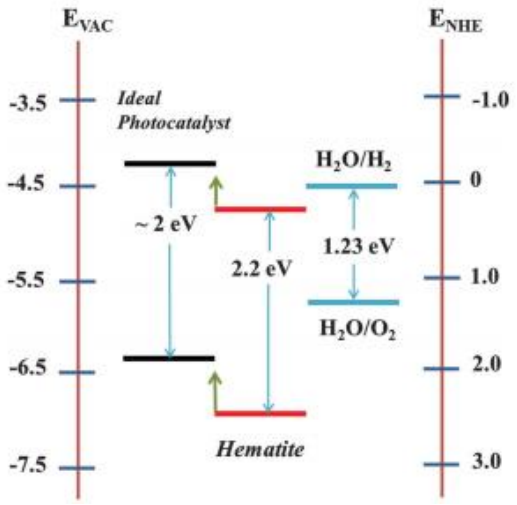

Figure 8: Schematic representation of band levels for hematite and for an ideal photocatalyst for water oxidation to hydrogen and oxygen.

Although the small band gap (2.1 eV) allows 15.3% of theoretical PEC efficiency under 1-sun irradiation, the conversion efficiency of Fe_2O_3 is low (ca.5 % up to date). Contributing factors are: (1) low mobility of carriers (~0.1 $cm^2 V^{-1} s^{-1}$), (2) short hole diffusion lengths, (3) low rate of water oxidation (poor catalysis), (4) high electron-hole recombination rates and (5) inhibited hydrogen evolution due to the conduction band energetics.[46, 47, 48]

To increase the photocurrent and the conversion efficiency of Fe_2O_3, many improved methods have been developed, nanostructuring advancements, doping, junction structure and surface modification have been used to lower the onset potential, improve the light absorption, accelerate the hole transport and improve catalysis.[44]

Doping is beneficial to enhance the bulk carrier concentration and the conductivity in many photoelectrochemical systems. Bare hematite has very low electrical conductivity, carrier concentration and electron mobility. Since the 70's, many elements have been used to dope Fe_2O_3 to enhance the photocurrent, as shown in Figure 9.[49]

Dopant	Concentration	Technique	Photoresponses
W	0.0025%	Synthesized ceramics	IPCE 29% at 400 nm and 1.23 V_{RHE}
Mo	15%	Electrodeposition	IPCE 12% at 400 nm and 1.4 V_{RHE}
V	0.05%	Synthesized ceramics	IPCE 28% at 400 nm and 1.23 V_{RHE}
Nb	0.5%	Synthesized ceramics	IPCE 27% at 400 nm and 1.23 V_{RHE}
Nb	0.1%	Synthesized ceramics	135 cm^{-2} at 0.2 V_{SCE} (100 W Hg arc lamp, 20 mW cm^{-2})
Nb	1.5%	Single crystal	IPCE 37% at 370 nm and 1.23 V_{RHE}
Nb	10%	Synthesized ceramics	IPCE 26.7% at 450 nm and 1.5 V_{RHE}
Ta	0.5%	Synthesized ceramics	IPCE 32% at 400 nm and 1.23 V_{RHE}
Ta	0.5%	Synthesized ceramics	640 μA cm^{-2} at 0.7 V (a high-pressure lamp of 1 KW) (two-electrode setup)
Si	2%	Synthesized ceramics	IPCE 34% at 400 nm and 1.23 V_{RHE}
Si	2%	Synthesized ceramics	IPCE 9.3% at 340 nm and 1.49 V_{RHE}
Si	~1.5%	APCVD	IPCE 42% at 370 nm and 1.23 V_{RHE}
Si	5.3%	RMS	IPCE 2.5% at 375 nm and 1.54 V_{RHE}
Si	0.1%	SP	IPCE 23% at 360 nm and 1.4 V_{RHE}
Si	0.2%	SP	0.37 mA cm^{-2} at 1.23 V_{RHE} (0.8 sun, AM 1.5)
Ti	5%	RMS	IPCE 14% at 375 nm and 1.54 V_{RHE}
Ti	4%	RBD	IPCE 31% at 360 nm and 1.4 V_{RHE}
Ti	2.5%	PVD	IPCE 15% at 360 nm and 1.6 V_{RHE}
Ti	1%	Synthesized ceramics	IPCE 1.2% at 340 nm and 1.49 V_{RHE}
Ge	0.05%	Synthesized ceramics	IPCE 5.5% at 340 nm and 1.44 V_{RHE}
Zr	0.5%	Synthesized ceramics	IPCE 23% at 400 nm and 1.23 V_{RHE}
Zr	2.0%	Electrodeposition	2.1 mA cm^{-2} at 1.64 V_{RHE} (Xe lamp, 150 mW cm^{-2})
Ru	5%	Synthesized ceramics	108 μA cm^{-2} at 0.2 V_{SCE} (100 W Hg arc, 20 mW cm^{-2})
Sn	4%	RBD	IPCE 21% at 360 nm and 1.4 V_{RHE}
Sn	0.05%	Synthesized ceramics	IPCE 4.0% at 340 nm and 1.04 V_{RHE}
Sn	4%	Deposition annealing	IPCE 0.7% at 420 nm and 0.3 V *vs.* Ag/AgCl (0.2 M NaOH)
Sn	9.4%	Hydrothermal method	IPCE 19.2% at 400 nm and 1.23 V_{RHE}

Figure 9: Photoresponses of some doped hematite photoelectrodes.[49]

When the oxidation state of the doped metals are not +3, such as Mg, Cu, Ni, Sn, Ti, Zr, Si replaces Fe^{3+} in the lattice, the dopants can act as electron donor or acceptor to increase the carrier density and potentially the current. Metals such as Sn, Ti, Zr and Si, are +4 dopants are electron donors when replacing Fe^{3+}.[44, 50, 51] Gratzel et al. reported that compared with pure Fe_2O_3, Si-doped hematite showed a higher photocurrent.[52] The Mott-Schottky analysis showed that the enhanced performance was attributed to the increased donor density. Deng *et al.* has reported a Ti doped urchin-like morphology hematite, a remarkable plateau photocurrent density value of 3.76 mA/cm^2 was observed at 1.74 V vs. RHE, which was 2.5 times higher than that for the pristine nanostructures (1.48 mA/cm^2).[53] When doped with +2 metal element, Mg, Cu, Ni could act as an electron acceptor.[54, 55, 56] Naghmehalsadat Mirbagheri and his co-workers found the donor density of Zn doped Fe_2O_3 is lower than Fe_2O_3, but it still showed a higher current.[57]

As stated above, the short hole diffusion length (2 – 4 nm) and low mobility of carriers in Fe_2O_3, allows nanostructuring asan efficient way to short the distancefrom the point of excitation to the reactive surface.

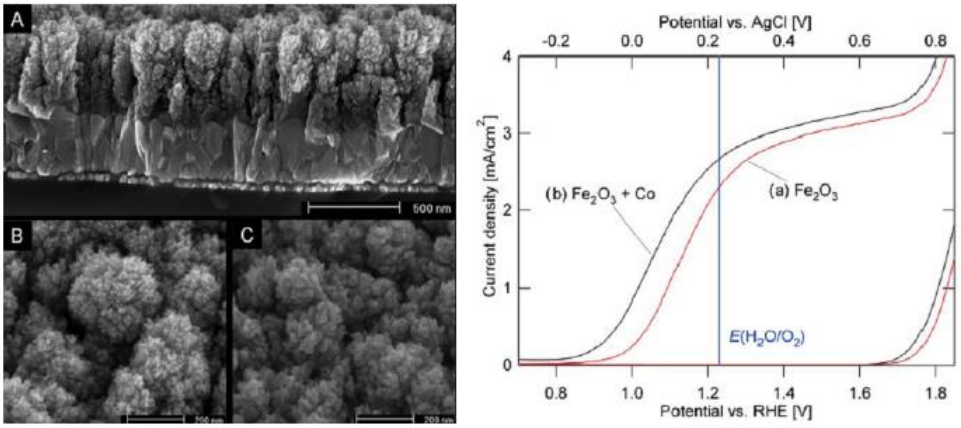

Figure 10: HR-SEM images and photoelectrochemical characteristics of Fe_2O_3 dendritic nanostructure films grown by APCVD.[58]

Gratzel *et al.* synthesized the dendritic nanostructure Fe_2O_3 films grown by APCVD as shown in Figure 10. HRSEM reveals a highly developed dendritic nanostructure of 500 nm thickness having a feature size of only 10-20 nm at the surface. The dendritic Fe_2O_3 films showed a higher efficiency (IPCE) and photocurrent (2.2 mA/cm^2 in AM1.5G(Air Mass 1.5 Global) sunlight of 1000 W/m^2 at 1.23 V RHE) than the single crystalline Fe_2O_3 electrodes.[58]

In 2012, Li *et al.* reported the porous semiconducting α-Fe_2O_3 nanowires synthesised by solution growth of α-$FeF_3 \cdot 3H_2O$ nanowires, as shown in Figure 11. The 400 nm thick hematite nanowire photoelectrode yielded a photocurrent density of 0.54 mA/cm^2 at 1.23 V vs RHE (AM 1.5 G, 100 mW/cm^2, pH = 13.6, 1 M NaOH).[59]

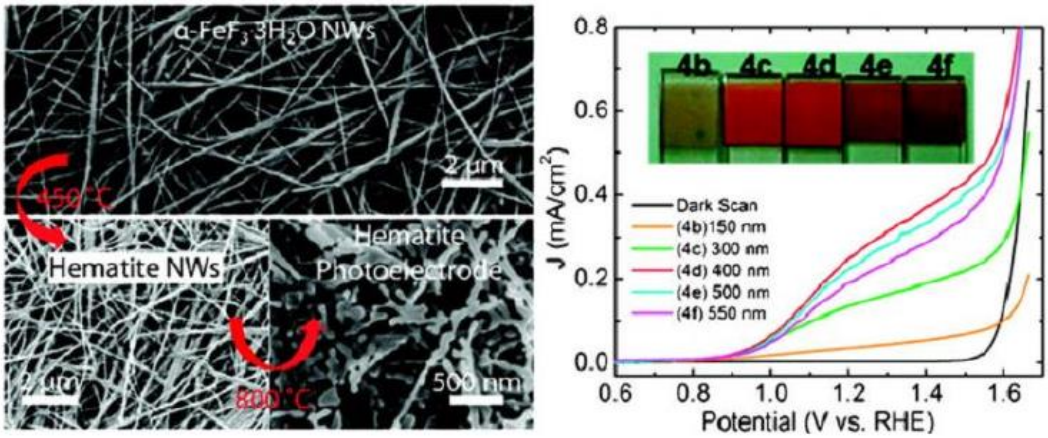

Figure 11: Preparation procedures and photocurrent densities of hematite nanowire photoelectrodes.[59]

As shown in Figure 12, Kim *et al*. presented a worm-like morphology of Pt doped hematite which resulted in photocurrent density 4.32 mA/cm^2 at 1.23 V vs. RHE which is the highest known.[60]

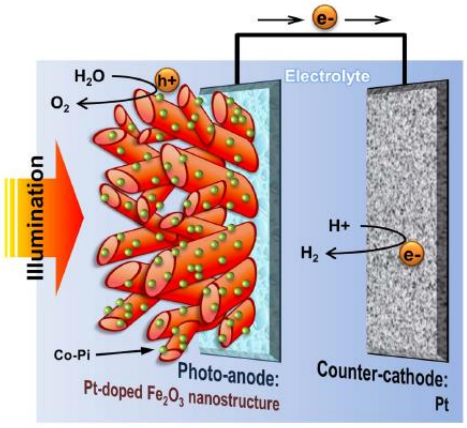

Figure 12: Schematic diagram for a photoelectrochemical cell with the hematite thin film photoanode.[60]

Surface modification is the most popular method to load a better water oxidation catalyst which can store the hole and increase the rate of water oxidation. Electrodeposited or photoelectrodeposited amorphous 'Co-Pi' on Fe_2O_3 as cocatalyst has been widely studied, since DK Zhong *et al.* found 'Co-Pi' could lower the onset potential and enhance the photocurrent of Fe_2O_3 in 2009.[61] Tilley et al. showed that IrO_2 nanoparticles loaded on the surface of a hematite photoanode can achieve the

negative shift of overpotential and obtain a higher photocurrent around 3.75 mA/cm^2.[47] Li Can and his co-workers modified Fe_2O_3 with IrO_2 and $Ni(OH)_2$ at the same time. They found after loading with IrO_2 and $Ni(OH)_2$, the LSV (Linear Sweep Voltammetry) data show a doubled current density compared to pure Fe_2O_3 and about 200 mV negative shift of the onset potential.[62]

Junction structures including heterojunction and homojunctions are a common method in photocatalysis and phtoelectrochemistry to enhance the photo-generated hole and photo-generated electron separation and inhibit the carrier recombination.[44] Some n-type metal oxides such as Al_2O_3, SnO_2 and ZnO and p-type metal oxides like NiO and n-type $CaFe_2O_4$ have been reported to modify the surface of Fe_2O_3 which could form n-n or p-n junctions to decrease the recombination of carriers and benefit the charge separation, as shown in Figure 13.[63, 64, 65, 66, 67]

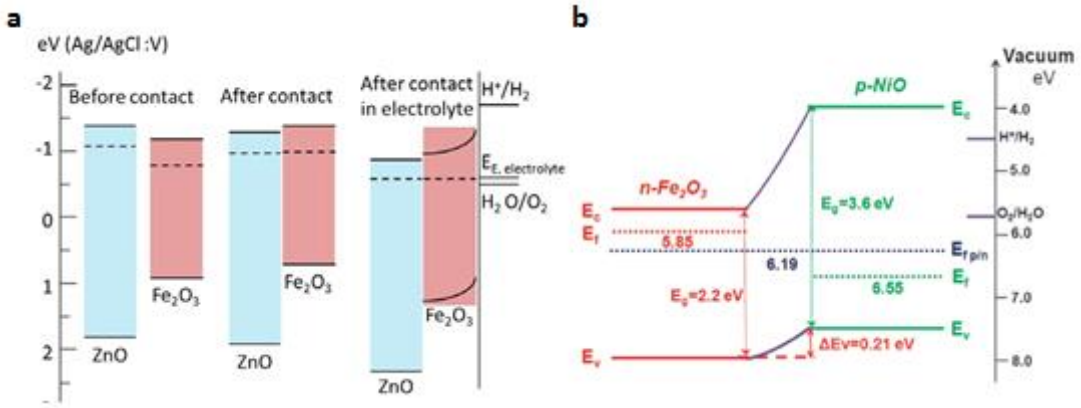

Figure 13: The mechanism of n-n heterojunction (a) and p-n heterojunction (b).

P. Feng and his co-workers fabricated a three-dimensional branched $Fe_2O_3/MgFe_2O_4$ heterojunction.[68] The photocurrent density of the heterojunction is 2.69 times higher than that of Fe_2O_3. The heterojunction showed an excellent charge transfer and enhanced light-harvesting ability. Kyoung-Shin Choi *et al.* showed the $Fe_2O_3/ZnFe_2O_4$ heterojunction significantly enhanced photocurrent response compared to the bare Fe_2O_3.[69]

In the process of heterojunction formation, energy level matching is one of the biggest challenges. Recently some reports about Fe_2O_3 p-n homojunctions have been constructed which could mitigate problems caused by energy mismatch between water redox potentials and the band edges of hematite and many other low-cost metal oxides, enabling practical solar water splitting as a means for solar energy storage, as shown in Figure 14.[56]

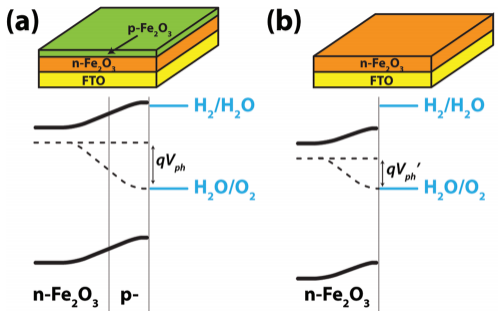

Figure 14: Energy band diagrams of hematite with a p-type coating.The p-type surface coating leads to a more negative band edge capable of reducing protons to hydrogen

1.8: Project Aims

As discussed in this chapter, there are many methods that could enhance the photoelectrochemical water splitting property of Fe_2O_3 based photoanodes. However, Fe_2O_3 still cannot meet requirements for practical application. Further improvement of Fe_2O_3 to achieve the solar energy to chemical energy transfer is required.

This thesis will describe the synthesis of two kinds of morphology of Fe_2O_3 by hydrothermal methods. Doping, homojunction structure and surface modification were used to enhance the property of Fe_2O_3 for photoelectrochemial water oxidation. The characterization and impact of these modifications has been analyzed by many physical chemistry methods.

The synthesis and characterization of Fe_2O_3 nanoparticles will be presented in chapter 2. Based on these nanoparticles, a new layered Co-doped Fe_2O_3/Sn-doped Fe_2O_3/FTO substrate (Co/Sn/Fe_2O_3) n-n homojunction photoanode was synthesized. The properties and mechanism of PEC water oxidation will be also be described.

In chapter 3, Fe_2O_3 nanorod arrays will be described. CdS and Cu_2O nanoparticles were synthesized and loaded on the surface of Fe_2O_3 nanorods by a chemical bath method. This three layer structure heterojunction photoanode improved the carrier transfer, decreased the self-oxidative decomposition of chalcogenide and enhanced the OER activity.

In chapter 4, UV light deposited amorphous CoO_x on the surface of Fe_2O_3 nanorods array will be described. The properties and mechanism of amorphous CoO_x cocatalyst on the Fe_2O_3 will be described including analysis by electrochemical impedance spectroscopy.

Chapter 2

High-performance of Co-doped Fe_2O_3/Sn-doped Fe_2O_3 n-n homojunction photoanode for photoelectrochemical water oxidation

2.1: Introduction

Recently some reports about Fe_2O_3 p-n homojunction have been constructed which could mitigate problems caused by energy mismatch between water redox potentials and the band edges of hematite and many other low-cost metal oxides, enabling practical solar water splitting as a means for solar energy storage.[56]

However, the band bending of p-type semiconductors at the electrolyte interface does not benefit hole accumulation on the surface which limits the rate of water oxidation[70, 71]. So coupling of different n-type Fe_2O_3 to form an n-n Fe_2O_3 homojunction is an effective strategy to enhance the separation of electron-hole pairs and improve the photoconversion efficiency.

Co doped Fe_2O_3 has been described by Hou and his co-workers. They found Co doped Fe_2O_3 could present a higher photocurrent compared with bare Fe_2O_3 as the donor density increases. A new Co^{2+} doped energy level was formed at the top of VB in Fe_2O_3.[72] However it should be noted that Co is also known as a cocatalyst.

There are many publications describing Sn-doped Fe_2O_3 photoanode. [46, 73]They found Sn^{4+} could act as an electron donor to increase the donor density and accelerate the carried transfer rate in the iron oxide and the interface between Fe_2O_3 and FTO. Unlike Co, the Sn-doped energy level was formed below the CB of Fe_2O_3.

2.2: Chapter Aims

Herein, we present the synthesis and characterization of a new layered Co-doped Fe_2O_3/Sn-doped Fe_2O_3/FTO substrate (Co/Sn/Fe_2O_3) n-n homojunction photoanode for efficient PEC water oxidation. A facile two step hydrothermal method for the fabrication of this n-n homojunction photoanode was developed, using $CoCl_2$•$6H_2O$,

$SnCl_4 \cdot 4H_2O$ and $FeCl_3$ as precursors. Fe_2O_3, Sn-doped Fe_2O_3 (Sn/Fe_2O_3), Co-doped Fe_2O_3 (Co/Fe_2O_3), and Sn-doped Fe_2O_3/Co-doped Fe_2O_3 ($Sn/Co/Fe_2O_3$) photoanode were synthesized as control samples. In comparison with the Fe_2O_3, Sn/Fe_2O_3, Co/Fe_2O_3 and $Sn/Co/Fe_2O_3$ photoanode, an enhancement of the photocurrent density at 1.23 V vs reversible hydrogen electrode (RHE) has been observed on the $Co/Sn/Fe_2O_3$ n-n homojunction photoanode. All of the as-prepared samples were characterized in detail by X-ray diffraction (XRD), Scanning Electron Microscopy (SEM), UV-Vis Transmission Spectroscopy, Photoelectrochemistry (PEC) and Electrochemical Impendence Spectroscopy (EIS).

2.3: Results and Discussion

2.3.1: Synthesis

Currently, the methods to synthesize Fe_2O_3 films include deposition from colloidal solutions, Ultrasonic Spray Pyrolysis, APCVD, hydrothermal deposition amongst others.[60] Compared with other methods, photoanodes synthesized by hydrothermal methods show the greatest photocurrents. The Fe_2O_3 nanoparticles in the film grow on the FTO directly which makes a clean interface between the FTO substrate and Fe_2O_3 nanoparticles[46]. The clean FTO was placed in a 20 mL hydrothermal reactor, with a 15 mL aqueous solution containing $FeCl_3$ (0.25 mmol). The autoclave was placed at 180 °C for 1.2 h. After cooling to room temperature, the product was collected and rinsed with deionized water and dried in a nitrogen atmosphere stream, and annealed in air at 550 °C for 2 h and 800 °C for 20 min. In our hydrothermal process the Fe_2O_3 nanoparticles cover both sides of FTO glass substrate, but the Fe_2O_3 nanoparticles on the non-FTO side were easily removed by washing with water. Samples were then heated at 550 °C for 2 hours to dry and crystallize the film followed by heating at 800 °C for 20 min to improve the connection between FTO film and Fe_2O_3 nanoparticles. The synthesis of Sn/Fe_2O_3 and Co/Fe_2O_3 was similar to Fe_2O_3 except that $SnCl_4 \cdot 5H_2O$ (0.005 mmol) and $CoCl_2 \cdot 6H_2O$ (0.002 mmol) was

added into the autoclave as dopant for hydrothermal reaction. $Co/Sn/Fe_2O_3$ was achieved using a two-step hydrothermal reaction. First, the clean FTO (1 cm × 3 cm) was placed in a 20 mL hydrothermal reactor, with a 15 mL aqueous solution containing $FeCl_3$ (0.25 mmol) and $SnCl_4•5H_2O$ (0.005 mmol). The autoclave was placed at 180 °C for 1.2 h using a ramp rate of 5 °C/min. The product was collected and rinsed with deionized water and dried in a nitrogen atmosphere stream, and annealed in air at 550 °C for 2 h. Then, the FTO coated with Sn/Fe_2O_3 was placed in an autoclave, with a 20 mL aqueous solution containing $FeCl_3$ (0.25mmol) and $CoCl_2•6H_2O$ (0.002 mmol). The autoclave was placed at 180 °C for 1.2 h using a ramp rate of 5 °C/min. The product was collected and rinsed with deionized water and dried in a nitrogen atmosphere stream, and annealed in air at 550 °C for 2 h and 800 °C for 20 min to obtain $Co/Sn/Fe_2O_3$ photoanode. The way to synthesize $Sn/Co/Fe_2O_3$ is identical but the order of Sn and Co processes is reversed. Photographs of Fe_2O_3, Co/Fe_2O_3, Sn/Fe_2O_3, $Sn/Co/Fe_2O_3$ and $Co/Sn/Fe_2O_3$ film on FTO glass are shown in Figure 15. The films appear homogeneous based on the photographs and SEM pictures which will be described in detail below. The color intensity of the films decreases in the order of $Sn/Co/Fe_2O_3$ > $Co/Sn/Fe_2O_3$ > Co/Fe_2O_3 > Fe_2O_3 > Sn/Fe_2O_3, to the naked eye. The films are adhered on the FTO and cannot be removed except by scraping with a knife.

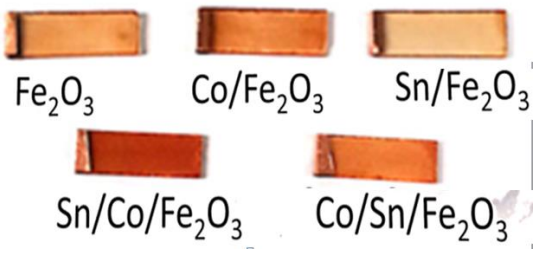

Figure 15: The photograph of Fe_2O_3, Co/Fe_2O_3, Sn/Fe_2O_3, $Sn/Co/Fe_2O_3$ and $Co/Sn/Fe_2O_3$

2.3.2: Structural characterisation

PXRD diffractograms of Fe_2O_3, Co/Fe_2O_3, Sn/Fe_2O_3, $Sn/Co/Fe_2O_3$ and $Co/Sn/Fe_2O_3$ are shown in Figure 16. All samples represent the typical crystal structure of FTO and hematite phase and no diffraction peak arising from metallic cobalt or cobalt oxides.[72, 74] Comparison of the PXRD patterns of photoanodes doped with and without Sn, no metallic Sn or Sn oxidescould be observed except for peaks which belong to FTO. These results indicate that the ratio of Co and Sn in the hematite is lower than the detection limits of PXRD, and the doped Co and Sn atoms are likely to be highly dispersed in the hematite and without any aggregation on the exterior of the Fe_2O_3 surface.[72, 75] Given the high temperatures used to process the films it is unlikely that amorphous material is present in high concentration.

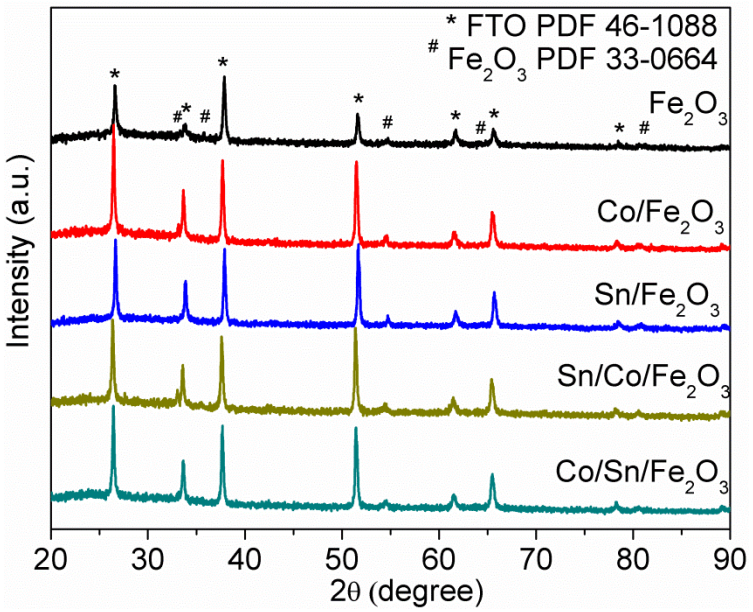

Figure 16: The XRD patterns of as-prepared Fe_2O_3, Co/Fe_2O_3, Sn/Fe_2O_3, $Sn/Co/Fe_2O_3$, and $Co/Sn/Fe_2O_3$ samples.

Morphological characteristics shown in Figure 17 and 18 illustrate the top view and cross-sectional structures of Fe_2O_3, Co/Fe_2O_3, Sn/Fe_2O_3, $Sn/Co/Fe_2O_3$ and $Co/Sn/Fe_2O_3$ which were characterized by field emission scanning electron microscopy (FE-SEM). All the samples appear homogeneous, and unlike most of the

literature prepared hydrothermally, these photoanodes were composed with Fe_2O_3 nanoparticles rather than nanorods, as shown in Figure 17.[76] The top view analysis show the size of Fe_2O_3 particles is about 100 nm and unchanged by doping with Co. Sn-doping appears to decrease the size of Fe_2O_3 nanoparticles to ca. 60 nm, which is similar to that previously reported.[77, 78, 79] From the side view of samples which are shown in Figure 18, there is a two-layer 'sandwich-like' structure observed for $Sn/Co/Fe_2O_3$ and $Co/Sn/Fe_2O_3$ but a single layer structure for Fe_2O_3, Co/Fe_2O_3 and Sn/Fe_2O_3. The thickness of a single layer in Fe_2O_3, Co/Fe_2O_3 and Sn/Fe_2O_3 is about 300 nm. For $Sn/Co/Fe_2O_3$ and $Co/Sn/Fe_2O_3$, the 'sandwich-like' structure has a thickness of ca. 550 nm composed from the first layer with 300 nm and second layer with 250 nm thickness. It is thus reasonable to believe that the intimate contact between the Co/Fe_2O_3 layer and Sn/Fe_2O_3 layer could form a homojunction to facilitate the separation of photogenerated carriers, consequently improving the PEC efficiency.

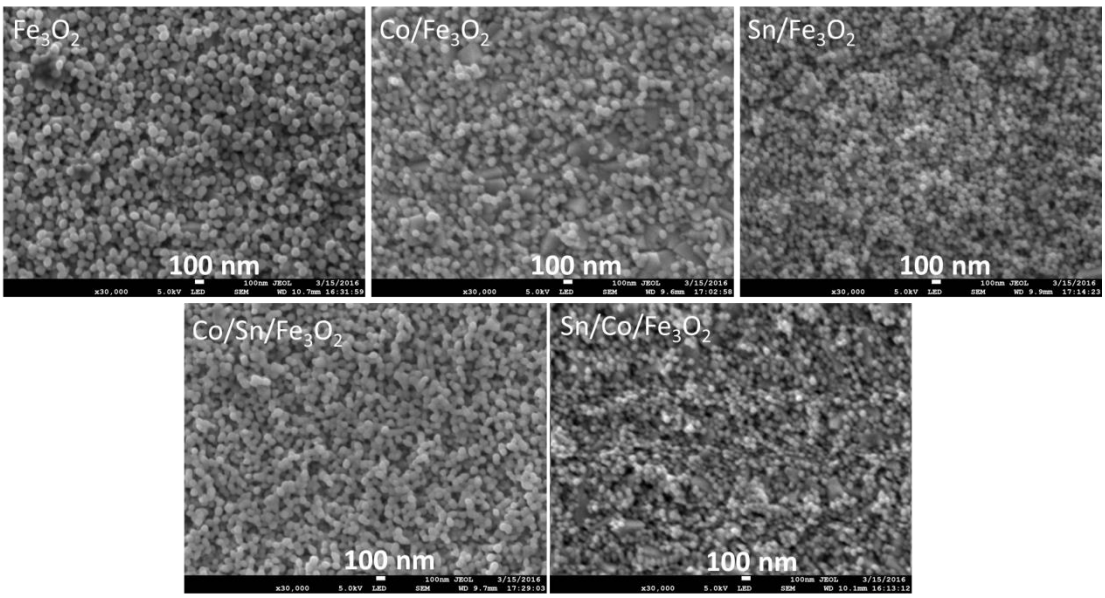

Figure 17：Scanning electron micrographs of the top view of the Fe_2O_3, Co/Fe_2O_3, Sn/Fe_2O_3, $Co/Sn/Fe_2O_3$ and $Sn/Co/Fe_2O_3$ samples.

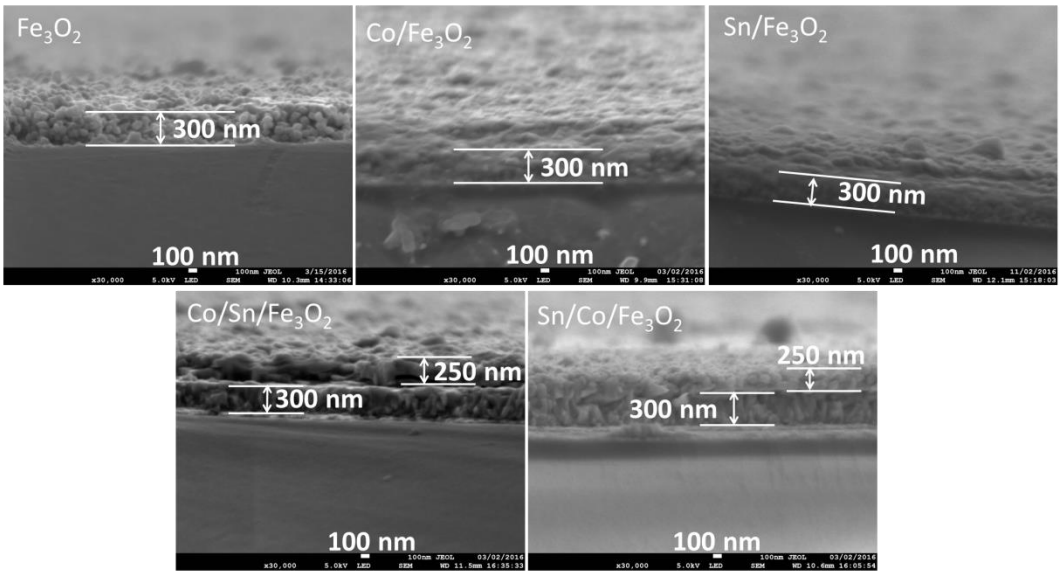

Figure 18: Scanning electron micrographs of the cross-section of the Fe_2O_3, Co/Fe_2O_3, Sn/Fe_2O_3, Co/Sn/Fe_2O_3 and Sn/Co/Fe_2O_3 samples.

2.3.3: Chemical state characterization

XPS was performed to confirm and characterize the chemical states of Sn and Co species in Co/Sn/Fe_2O_3. The XPS spectra are shown in Figure 19.

The Fe *2p* in Figure 19A, the $2p_{3/2}$ and $2p_{1/2}$ core levels of Fe species are discerned at around 710.7 and 724.1 eV, respectively. This indicates that the Fe species in Co/Sn/Fe_2O_3 is in the +3 oxidation state.[46]

From the Sn *3d* XPS spectra (Figure 19B), we could easily identify the peak position of $3d_{5/2}$ and $3d_{3/2}$ binding energies of tin, which are around 486.6 and 495.2 eV, respectively. The difference between the two values is equal to 8.5 eV. This demonstrates that Sn is in the +4 oxidation state in Co/Sn/Fe_2O_3.[75]

The Co chemical state was measured by XPS, shown in Figure 19C. It is easy to identify the peaks between 775.8 and 795 eV which could be assigned to 2p of Co species. Qnatitative analysis of the spectrum shows that the Co species exist with +2 and +3 oxidation states and the ratio is 1:3. [72]

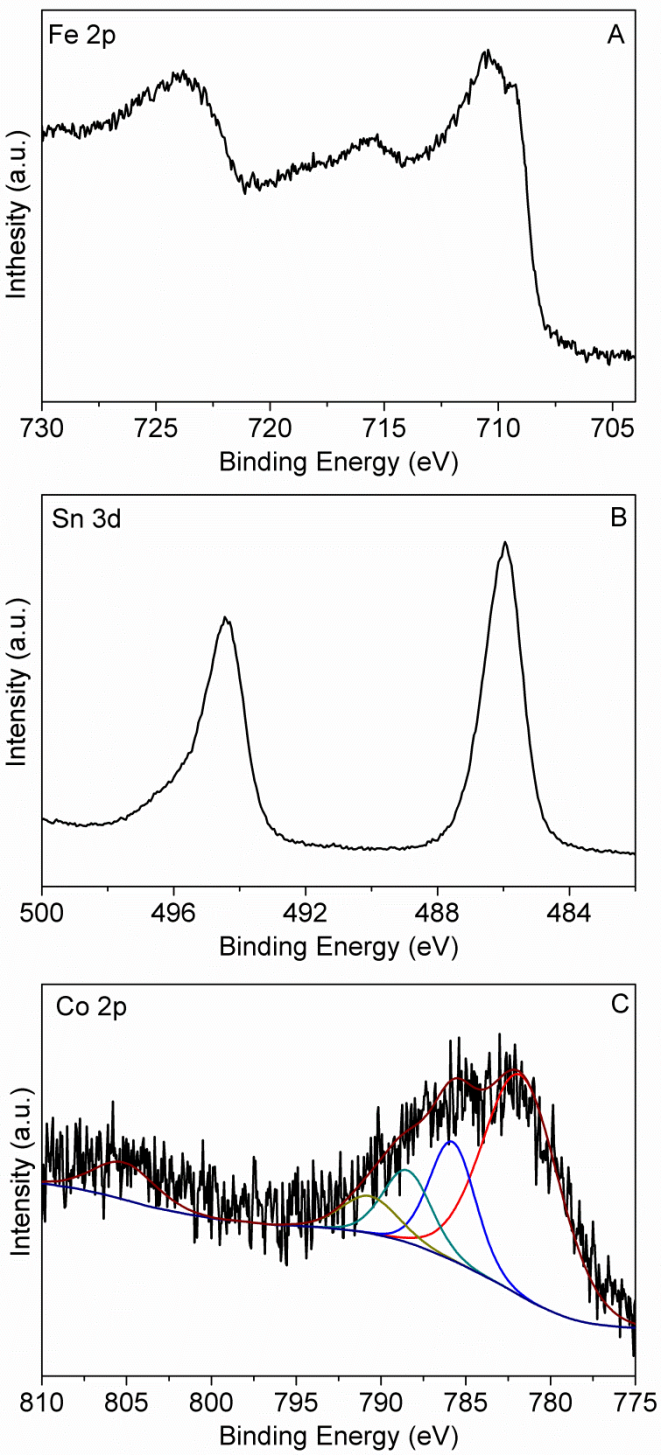

Figure 19: The high-resolution core XPS spectra of (A) Fe2p, (B)Sn 3d and (C) Co 2p of Co/Sn/Fe_2O_3.

2.3.4: UV-vis spectroscopy

The UV-vis spectrums of Fe_2O_3, Co/Fe_2O_3, Sn/Fe_2O_3, $Sn/Co/Fe_2O_3$, $Co/Sn/Fe_2O_3$ are shown in Figure 20. The band edge absorption of pure Fe_2O_3 is at ca. 610 nm, whereas the absorption of Sn/Fe_2O_3 shifted to shorter wavelength (ca. 20 nm). This behaviour which could be due to the Sn doping is in good agreement with the effect of particle size quantization on indirect bandgap of hematite, which suggests that the quantum size effect can be partly responsible for the increase of the bandgap of hematite, which echo the result of SEM. However, the particles are too large for quantum size effects. More likely the Sn atoms occupy defect sites which are responsible for the Urbach Tail.[80, 81, 82] In contrast the edge shifts toward long wavelength for Co/Fe_2O_3, and Yang *et al.* found the doping of Co could introduce an impurity level which lay above the valence band of Fe_2O_3.[72] This red-shift in light absorption could be attributed in part to a transition of charge-transfer between the cobalt ions and the conduction or the valence band of Fe_2O_3. Furthermore, compared with single layer Fe_2O_3, $Co/Sn/Fe_2O_3$ and $Sn/Co/Fe_2O_3$ samples showed a remarkable red-shift in the band-edge absorption. The markedly enhanced absorption before the absorption edge is discernible which could be due to the thickness of the samples. These results are in accordance with the naked eye, shown in Figure 15.

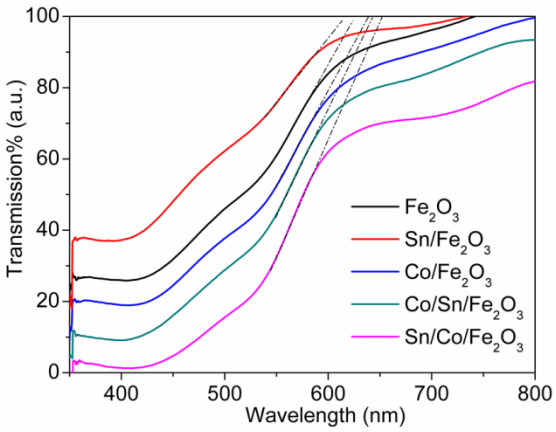

Figure 20: The UV-vis transmission spectra of Fe_2O_3, Sn/Fe_2O_3, Co/Fe_2O_3, $Co/Sn/Fe_2O_3$ and $Sn/Co/Fe_2O_3$.

2.3.5: Photoelectrochemical Performance for Water Oxidation

The PEC performance of the photoanodes was obtained in 1 M NaOH electrolyte under visible light irradiation (λ > 420 nm). The measured potentials vs Ag/AgCl were converted to the reversible hydrogen electrode (RHE) scale according to the Nernst equation, as shown in Equation 2:

$$E_{RHE} = E_{Ag/AgCl} + 0.059pH + E^{0}_{Ag/AgCl}$$

Where E_{RHE} is the converted potential vs RHE, $E^{o}_{Ag/AgCl}$ = 0.1976 V at 25^{o}C, and $E_{Ag/AgCl}$ is the experimentally measured potential against at Ag/AgCl reference.[46] Figure 21A shows the current density-potential (j-V) curves of Fe_2O_3, Co/Fe_2O_3, Sn/Fe_2O_3, Sn/Co/Fe_2O_3 and Co/Sn/Fe_2O_3 as working electrodes. The dark current densities in all cases are negligible (< 20 μA/cm^{-2}). Under visible irradiation, Fe_2O_3 yielded a photocurrent density of 0.5 mA/cm^2 at 1.23 V vs RHE. Compared to the pure Fe_2O_3 photoelectrode, the photocurrent density of Sn doped Fe_2O_3 and Co doped Fe_2O_3 show an impressive enhancement to 0.7 mA/cm^2 and 0.95 mA/cm^2 at 1.23 V vs RHE, respectively. A tremendous improvement for the photocurrent density at 1.23V vs RHE is achieved over the Sn/Co/Fe_2O_3 and Co/Sn/Fe_2O_3 photoanode under visible light irradiation compared to those of pure Fe_2O_3, Co/Fe_2O_3 and Sn/Fe_2O_3. The photocurrent density of Co/Sn/Fe_2O_3 photoanode at 1.23V vs RHE reached 1.6 mA/cm^2 whereas the photocurrent density of Sn/Co/Fe_2O_3 is 1.1 mA/cm^2 which indicate a better charge generation, separation, and transport occurred and could be attributed to the formation of the homojunction. In addition, for Co/Fe_2O_3 the onset potential of water oxidation in the anodic polarization curve moves to lower potential, this result is highly consistent with the DRS results above and literature, further validating that the doping of Co could introduce an impurity level above the VB of Fe_2O_3 and improve the oxidation capacity of Fe_2O_3.[72] However, the photoanodes containing Sn showed a positive shift of photo onset potential which means the water

oxidation kinetics is limited.[46, 51, 73] The on/off photocurrent response under visible light, which is also shown in Figure 21B, confirms the aforementioned results. The photocurrent intensity at 1.23V vs RHE decreases in the order of Co/Sn/Fe_2O_3 > Sn/Co/Fe_2O_3 > Co/Fe_2O_3 > Sn/Fe_2O_3 > Fe_2O_3 under visible light irradiation. All photoanodes show substantially stable performance, as shown in Figure 21C.

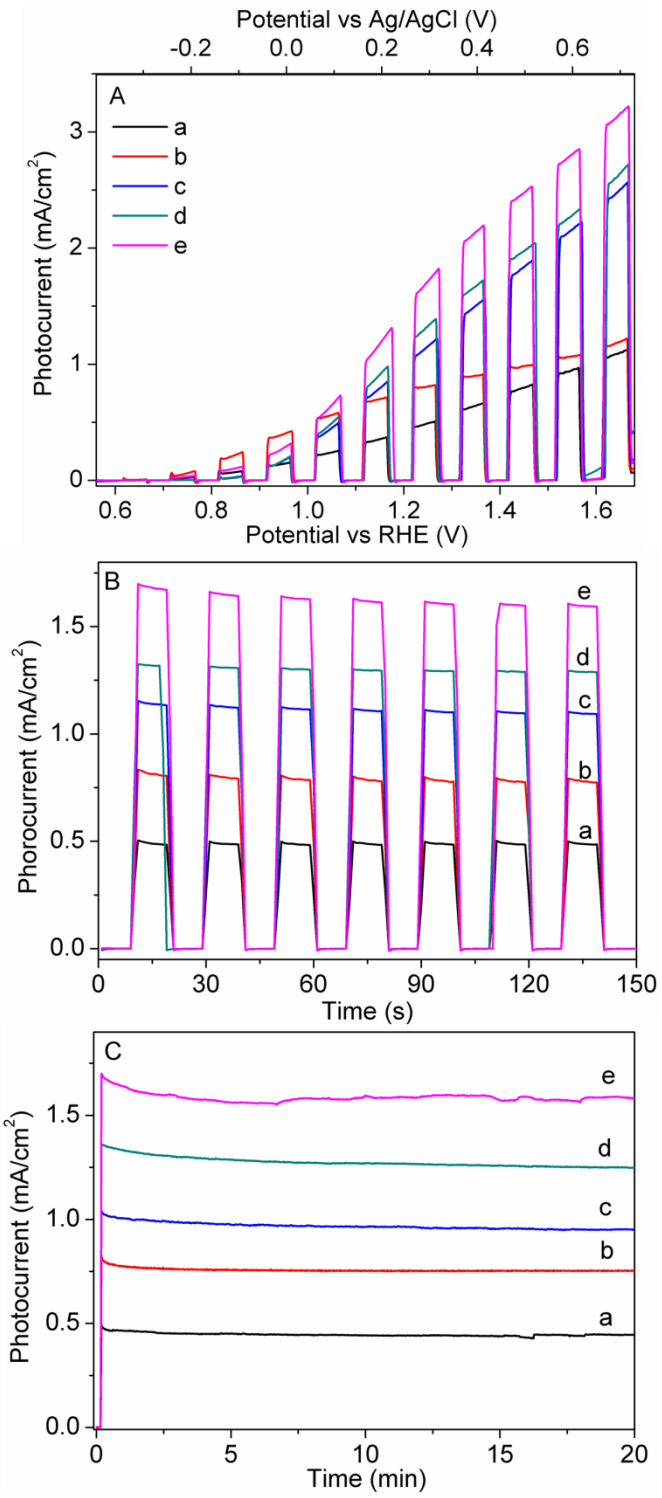

Figure 21: (A) Current density-potential (j-V) curves of (a)Fe_2O_3, (b)Sn/Fe_2O_3, (c)Co/Fe_2O_3, (d)$Co/Sn/Fe_2O_3$ and (e)$Sn/Co/Fe_2O_3$ under 1-sun irradiation(AM 1.5G, 100mW/cm^2); (B) The periodic on/off photocurrent response and (C) stable performance of (a)Fe_2O_3, (b)Sn/Fe_2O_3, (c)Co/Fe_2O_3, (d)$Co/Sn/Fe_2O_3$ and (e)$Sn/Co/Fe_2O_3$ at 1.23V vs RHE under 1-sun irradiation(AM 1.5G, 100mW/cm^2).

2.3.6: Impedance characteristics

To further understand the enhanced water oxidation property of the homojunction, we conducted a Mott-Schottky analysis and EIS measurements for the Fe_2O_3, Co/Fe_2O_3, Sn/Fe_2O_3, $Sn/Co/Fe_2O_3$ and $Co/Sn/Fe_2O_3$. Figure 22 displays the Mott-Schottky (M-S) plot for all hematite thin films recorded under dark condition. All hematite thin films are typical n-type semiconductor based on the positive slope of all samples in the M-S plot.[51, 72, 83] The donor densities and flat band potential of the Fe_2O_3, Co/Fe_2O_3, Sn/Fe_2O_3, $Sn/Co/Fe_2O_3$ and $Co/Sn/Fe_2O_3$ electrodes have been obtained from the slope of these plots based on the M-S equation, as shown in Table 1. N_D value analysis show the donor density decreases in the order of $Sn/Co/Fe_2O_3$ > $Co/Sn/Fe_2O_3$ > Co/Fe_2O_3 > Sn/Fe_2O_3 > Fe_2O_3. Fe_2O_3 shows the lowest donor density among all photoanode and the doping of Sn and Co will increase the donor density of hematite film. These data provided direct evidence to support that the Sn-doping and Co-doping served as an electron donor. Compared with some p-n junctions which have been published, such as p-NiO/n-hematite heterojunction electrode and p-$CaFe_2O_4$/n-hematite which would form a depletion layer to trap the electrons and holes and decrease the N_D, the n-n homojunction which comprises Sn/Fe_2O_3 and Co/Fe_2O_3 increases the N_D which enhance the photocurrent response at higher potential.[63, 84] In theory, the onset potential is assumed to be approximately equal to the flatband potential.[85] As shown in the table 1, the flatband potential of Co-doping Fe_2O_3 is lowest among all photoanodes. In contrast, clearly the addition of Sn promotes a significant anodic shift of the flat potential in relation to the undoped film. Ricardo H *et al.* found the increase in the V_{FB} maybe be associated with Sn enrichment in the hematite grain surface.[86]

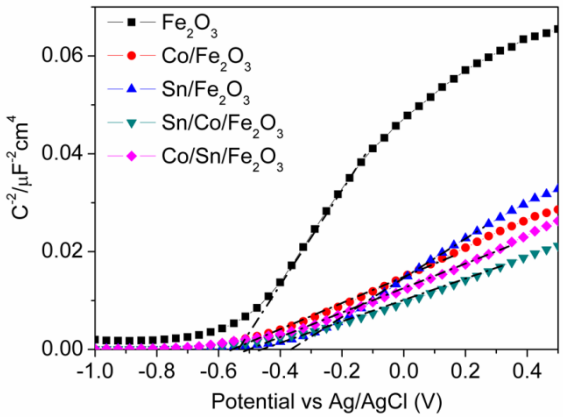

Figure 22: The Mott-Schottky plots of Fe_2O_3, Co/Fe_2O_3, Sn/Fe_2O_3, $Sn/Co/Fe_2O_3$ and $Co/Sn/Fe_2O_3$.

Table 1: Mott–Schottky parameters of Fe_2O_3, Co/Fe_2O_3, Sn/Fe_2O_3, $Sn/Co/Fe_2O_3$ and $Co/Sn/Fe_2O_3$

Sample	Flat Potential (V vs Ag/AgCl)	Donor Density x 10^{18} (cm^{-3})
Fe_2O_3	-0.53	18.67
Co/Fe_2O_3	-0.57	44.56
Sn/Fe_2O_3	-0.36	35.81
$Sn/Co/Fe_2O_3$	-0.47	83.48
$Co/Sn/Fe_2O_3$	-0.52	75.27

To gain further insight into the underlying mechanism, the Nyquist plots of Fe_2O_3, Co/Fe_2O_3, Sn/Fe_2O_3, $Sn/Co/Fe_2O_3$ and $Co/Sn/Fe_2O_3$ electrodes were measured at 1.23 V vs RHE.

In dark condition, a semicircle with different radius is clearly visible for all photoanodes which is associated with the charge-transfer process and a smaller radius correlated with a lower charge-transfer resistance, as shown in Figure 23.[86] Fe_2O_3 shows the largest radius, then followed by $Sn/Co/Fe_2O_3$, Co/Fe_2O_3 and $Co/Sn/Fe_2O_3$, and Sn/Fe_2O_3 show the lowest radius.

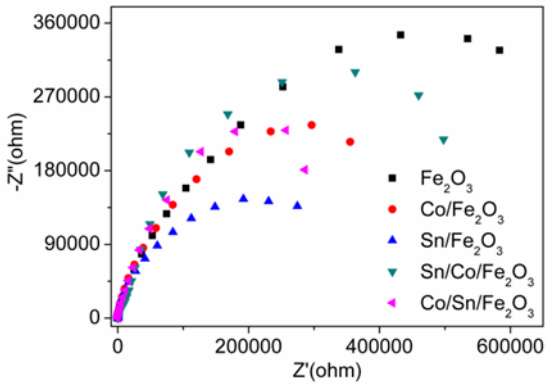

Figure 23: Nyquist plots of Fe_2O_3, Co/Fe_2O_3, Sn/Fe_2O_3, $Sn/Co/Fe_2O_3$ and $Co/Sn/Fe_2O_3$. The EIS spectra were measured in 1.0 M NaOH at 1.23 V vs RHE in dark condition.

The Nyquist plots of Fe_2O_3, Co/Fe_2O_3, Sn/Fe_2O_3, $Sn/Co/Fe_2O_3$ and $Co/Sn/Fe_2O_3$ measured under 1-sun light illumination can be seen in Figure 24. For Fe_2O_3, Co/Fe_2O_3, Sn/Fe_2O_3 and $Sn/Co/Fe_2O_3$, one semicircle is clearly visible. However, two semicircles are for $Co/Sn/Fe_2O_3$ electrode. According to the literature, the semicircle in high frequency can be attributed to the grain boundary impedance between FTO and Sn/Fe_2O_3, and the low frequency semicircle belongs to the remainder of the electrode.[87] For the lower frequency electrode impedance, the radius of the semicircle decreases with the order Fe_2O_3 > Co/Fe_2O_3 > Sn/Fe_2O_3 > $Sn/Co/Fe_2O_3$ > $Co/Sn/Fe_2O_3$, which means $Co/Sn/Fe_2O_3$ show the lowest resistance under light irradiation. For more detailed analysis, the experimental EIS data under 1-sun irradiation were fitted to an equivalent circuit model (EC), (Figure 24), using the EIS spectrum analyzer software. The fitted impedance parameter values of the resistances (R) and constant phase elements (CPE) are listed in Table 2.

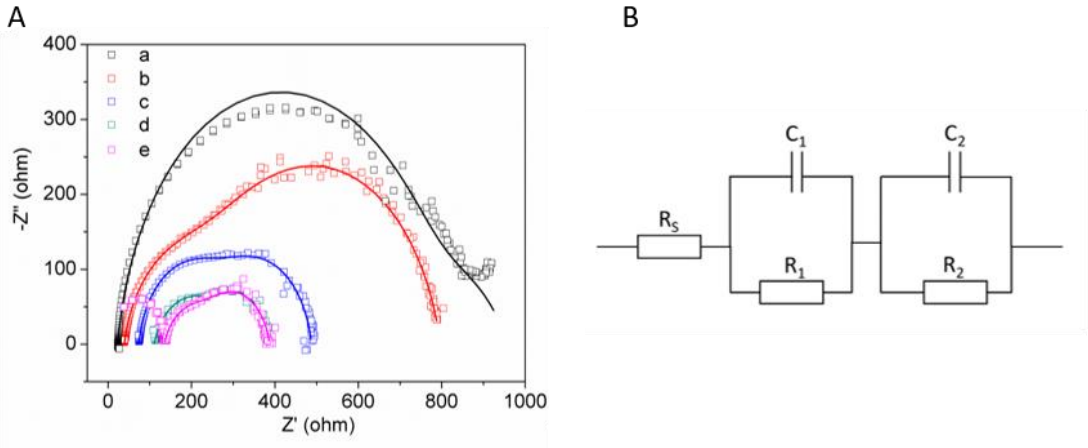

Figure 24: (A) Nyquist plots of Fe_2O_3 (a), Co/Fe_2O_3 (b), Sn/Fe_2O_3 (c), $Sn/Co/Fe_2O_3$ (d) and $Co/Sn/Fe_2O_3$ (e), (B) equivalent circuit model for Fe_2O_3, Co/Fe_2O_3 and Sn/Fe_2O_3 (c) and (C) equivalent circuit model for $Sn/Co/Fe_2O_3$ and $Co/Sn/Fe_2O_3$. The EIS spectra were measured in 1.0 M NaOH at 1.23 V vs RHE under 1-sun irradiation.

Table 2: Resistance and CPE Values Obtained by Fitting the EIS Spectra.

Sample	$R_s(\Omega)$	C_1 (μF)	$R_1(\Omega)$	C_2 (μF)	R_2 (Ω)
Fe_2O_3	23.21	1388	195	14.78	759.2
Co/Fe_2O_3	39.45	19.47	299.4	160.7	467.28
Sn/Fe_2O_3	90.34	13.82	215	156	183
$Sn/Co/Fe_2O_3$	113	29.28	115.1.1	239	160
$Co/Sn/Fe_2O_3$	136	19.7	137.4	280.1	114.78

As shown in the table 2, the values of R_1 and C_1 and R_2 and C_2 is the resistance and capacitance of bottom layer and top layer in Fe_2O_3 anode, respectively. The doping of Sn and Co improves the electronic conductivity of hematite, and the homojuntion, especially $Co/Sn/Fe_2O_3$, which has advantages for enhancing the carrier transfer. The lower R_1 and R_2 values further facilitate charge transfer of holes to the donor species in solution and suppress the recombination of photogenerated electron-hole pairs to improve the photocurrent.[46] A larger capacitance implies that more carries can be accumulated. The larger capacitance(C_2) in surface layer facilitates the participation of holes in the oxidation process. The value of C_2 in Sn/Fe_2O_3 and $Sn/Co/Fe_2O_3$ is smaller than Co/Fe_2O_3 and $Co/Sn/Fe_2O_3$, respectively. This indicates that, compared

with Sn doped layer, a Co doped layer could be more favourable for the PEC water oxidation.

2.3.7: IPCE measurements

For photoelectrochemical processes, the incident photon-to-current conversion efficiency (IPCE) is used to determine the wavelength dependence of the efficiency of the photoelectrode. This efficiency can be defined by Equation 3 below.

$$\textit{Equation 3: } IPCE\% = \frac{1240 \times I(mA/cm^2)}{\lambda(nm) \times P(mW/cm^2)} \times 100$$

Where I is photocurrent density, λ and P is the wavelength and light intensity of incident light, respectively. The incident photon-to-current efficiencies (IPCE) of the Fe_2O_3, Co/Fe_2O_3, Sn/Fe_2O_3, $Sn/Co/Fe_2O_3$ and $Co/Sn/Fe_2O_3$ photoanodes have been measured under monochromatic light irradiation and plotted as a function of wavelength at 1.23 V vs RHE, as shown in Figure 25.

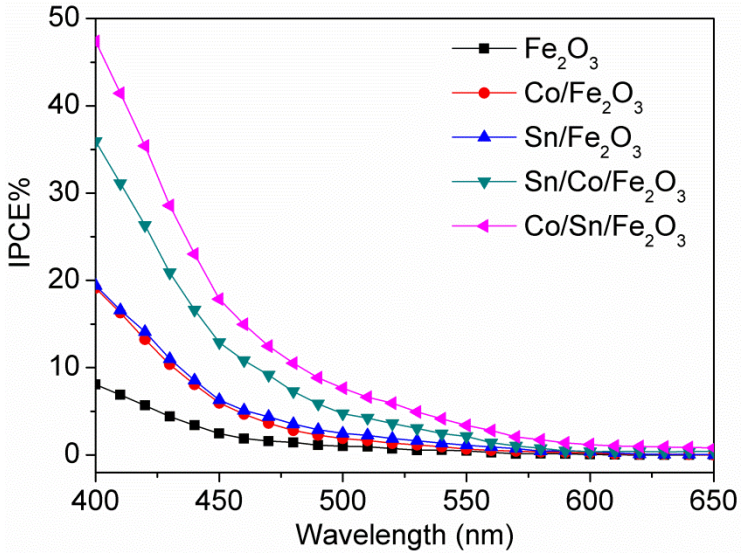

Figure 25: IPCE performance of Fe_2O_3, Co/Fe_2O_3, Sn/Fe_2O_3, $Sn/Co/Fe_2O_3$ and $Co/Sn/Fe_2O_3$ photoanode at 1.23V vs RHE.

The IPCEs for all samples showed the same tendency, with a sharp drop as the wavelength increases. The Co/Sn/Fe_2O_3 photoanode presents the highest efficiency which was measured to be above 10% for the incident light wavelength shorter than 500 nm. The IPCE value decreases in the order of Co/Sn/Fe_2O_3 > Sn/Co/Fe_2O_3 > Co/Fe_2O_3 $\approx$ Sn/Fe_2O_3 > Fe_2O_3, which confirms the aforementioned results that we obtained from PEC test.

2.4: Conclusions

We investigated the layer structure n-n homojunction composite anode of Co/Sn/Fe_2O_3 to enhance the photoactivity of Fe_2O_3. The composite electrode showed the highest photocurrent with ca. 2.5 times enhancement relative to bare Fe_2O_3, and 70% relative to Sn/Fe_2O_3 and Co/Fe_2O_3 at 1.23V vs RHE. The effect was revealed by electrochemical impedance spectroscopy analysis. The EIS study demonstrated n-n homojunction Co/Sn/Fe_2O_3 could increase the density of carriers, and improve the charge separation and reduce resistance in the charge transfer across the electrode and electrolyte. Thus fabrication of n-n Fe_2O_3 homojunction is an efficient method to enhance the performance of electrode for water splitting in PEC cells.

Chapter 3

Photoelectrochemical water splitting by a $Cu_2O/CdS/Fe_2O_3$ nanorod array photoanode stablized with Cu_2O as a hole transfer relay

3.1: Introduction

In this chapter, a new three layer structure heterojunction photoanode consisting of cupric oxide, cadmium sulfide and iron oxide, was synthesized aiming to improve the carrier transfer, decrease the self-oxidative decomposition of chalcogenide and enhance the OER activity.

Many publications have described that vertically aligned Fe_2O_3 nanowire arrays can show a better activity compared with Fe_2O_3 nanoparticles, which works as the electron conductor for direct charge transfer to FTO glass.[44, 48, 58, 88, 89]

CdS is an n-type semiconductor which has been widely used in photocatalytic reactions because of the small band gap (2.3 eV) and long diffusion length of photo-generated carriers.[90, 91] However, CdS is unstable and easy to oxidize by the photogenerated holes under light irradiation.[92]

As mentioned above, a junction constructed on the surface is a good method to improve photocatalytic performance of Fe_2O_3. Some literature describes that a heterojunction composed of Fe_2O_3 and CdS would show a better photoactivity, because the junction could enhance the separation of photo-generated carriers.[93, 94] However, the typical Fe_2O_3/CdS photocatalysts are used for WOC decomposition, such as methyl blue. Currently, Fe_2O_3/CdS has never been used as a photoanode because of the instability of CdS.

Cu_2O is a semiconductor with a direct bandgap of 2.1 eV. With the conduction band lying negative of the hydrogen evolution potential and the valence band lying just positive of the oxygen evolution potential, Cu_2O has been used in different photocatalystic reaction, like OER, HER, CO_2 reduction and so on but can also suffer

from degradation. [95, 96, 97] Zhu and his co-workers prepared Cu_2O/TaON heterojunction photoanode for PEC water splitting.[97]

3.2: Chapter aims

The aim of this chapter is to investigate if the Cu_2O layer could extract the hole from CdS layer to stabilize the CdS/Fe_2O_3 and release O_2 from water as shown in Figure 26.

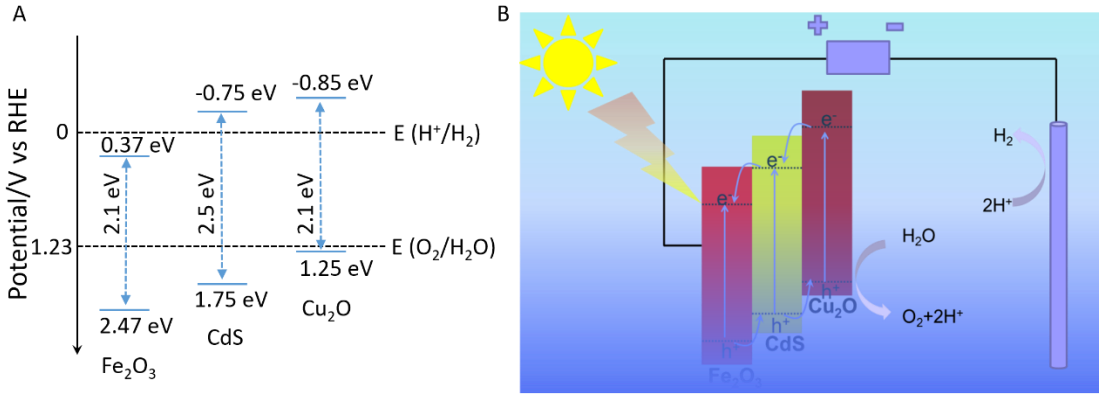

Figure 26: (A) The band structure of Fe_2O_3, CdS and Cu_2O and (B) possible mechanism of the three layers heterojunction.

In this chapter, the synthesis and characterization of a Cu_2O/CdS/Fe_2O_3 ternary composite photoanode will be presented. A facile three step method for the fabrication of this photoanode was developed. Fe_2O_3, CdS/Fe_2O_3, and Cu_2O/Fe_2O_3 photoanodes were synthesized as control samples. In comparison with the Fe_2O_3, CdS/Fe_2O_3, and Cu_2O/Fe_2O_3 photoanode, an enhancement of the photocurrent density at 1.23 V vs reversible hydrogen electrode (RHE) has been observed on the Cu_2O/CdS/Fe_2O_3 ternary layer photoanode. In this Cu_2O/CdS/Fe_2O_3 photoanode, the CdS acts as a hole transfer bridge between Cu_2O and Fe_2O_3 to achieve photo-generated hole output from Fe_2O_3 to Cu_2O for water oxidation reaction, the Cu_2O serves as a protective layer to extract the hole from CdS to decrease the decomposition of CdS and provide activite sites to release O_2 from water.

All of the as-prepared samples were characterized in detail by X-ray diffraction (XRD), Scanning Electron Microscopy (SEM), UV-Vis Transmittance Spectrum, Photoelectrochemistry (PEC) and Electrochemical Impendence Spectroscpoy (EIS).

3.3: Result and discussion

3.3.1: Synthesis of $Cu_2O/CdS/Fe_2O_3$ nanorod arrays

The Fe_2O_3 nanorod arrays were prepared by a modified literature report.[76] The clean FTO and high concentration $FeCl_3$ (0.15 M) was placed in a hydrothermal reactor, and heated at 100 °C for 6 h After cooling to room temperature, the product was collected and rinsed with deionized water and dried in a nitrogen atmosphere stream, and annealed in air at 550 °C for 2 h and 800 °C for 20 min.

As the interfacial energy between the crystal and the FTO substrate is smaller than the interfacial energy between the crystal and the solution, nuclei prefer to stick on the FTO substrate. When the reaction happens at a low temperature, the growth rate is controlled, and epitaxial crystal growth will take place from these nuclei, along the easy direction of crystallization. As the high concentration of $FeCl_3$, nanorods perpendicular to the substrate will be generated.[76]

The method for deposition of CdS and Cu_2O on Fe_2O_3 nanorod arrays by SILAR was modified according to a previous literature report.[97, 98] Fe_2O_3 nanorod arrays were first coated with CdS through the reaction between $Cd(Ac)_2$ and Na_2S solution Then the obtained CdS/Fe_2O_3 was stand in $Cu(Ac)_2$ solution and NaOH, successively. Then the electrode was finally heated under argon at 500 ^oC for 2h with a ramp rate of 10 ^oC min^{-1} to obtain $Cu_2O/CdS/Fe_2O_3$ nanorod arrays.

3.3.2: Structural characteristics

The XRD pattern of the samples Fe_2O_3, CdS/Fe_2O_3, Cu_2O/Fe_2O_3 and $Cu_2O/CdS/Fe_2O_3$ are shown in Figure 27. All samples show the typical crystal structure of FTO (JCPDS 46-1088) and the single-crystal nature of the Fe_2O_3 (JCPDS 33-0664) nanorods with (110) direction.[63] Some weak diffraction peaks which belong to CdS (JCPDS 64-3414) and Cu_2O (JCPDS 05-667) could be indexed after the coating of CdS and Cu_2O on the Fe_2O_3.[94, 97] These results mean that the Fe_2O_3 nanorod arrays, CdS and Cu_2O have been synthesized on the FTO glass successfully.

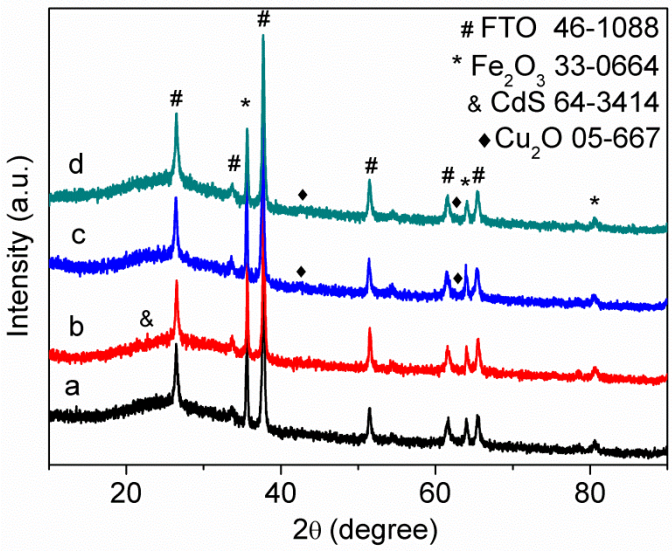

Figure 27: The XRD patterns of as-prepared Fe_2O_3 (a) CdS/Fe_2O_3 (b), Cu_2O/Fe_2O_3 (c)and $Cu_2O/CdS/Fe_2O_3$(e) samples.

3.3.3: Morphological characteristics

Figure 28 shows the cross-sectional image of the Fe_2O_3 nanorod arrays. We could observe that the vertical Fe_2O_3 nanorods were homogeneously grown and dispersed on FTO glass with diameter around 100 nm and length 500 nm.

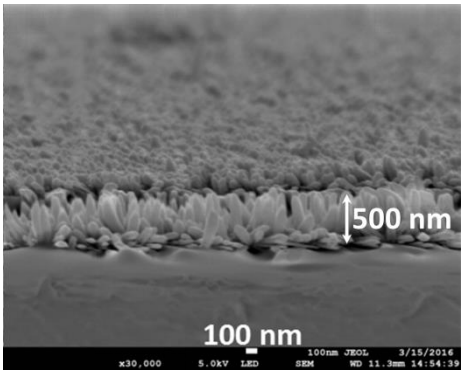

Figure 28: The Scanning electron micrograph of the cross-section of the Fe_2O_3 nanorods.

Figure 29 shows the top-view analyses of the Fe_2O_3 and $Cu_2O/CdS/Fe_2O_3$ nanorod arrays. Compared with the nanorod Fe_2O_3 image, SEMof $Cu_2O/CdS/Fe_2O_3$ the surface is rougher and there are some small features on the surface of Fe_2O_3. However, from the SEM image, it is hard to unambiguously identify the Cu_2O and CdS nanoparticles.

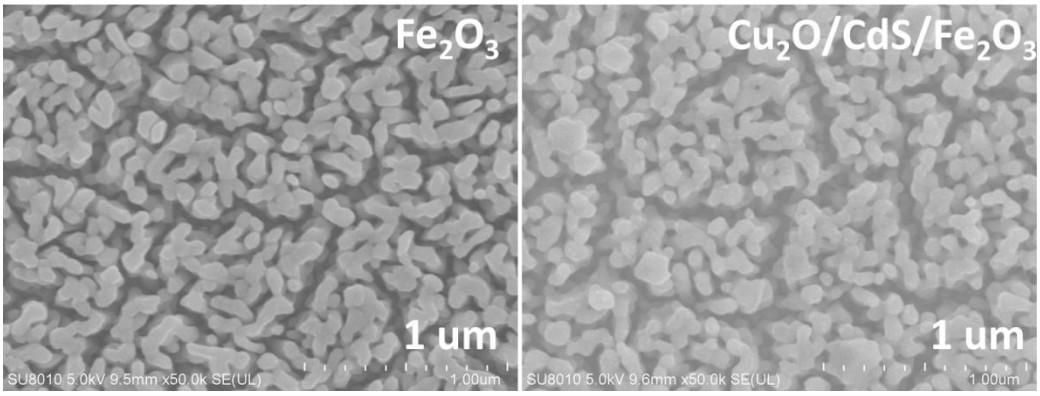

Figure 29: The Scanning electron micrographs of the top view of the Fe_2O_3 and $CdS/Cu_2O/Fe_2O_3$ nanorods.

Transmission electron microscopy (TEM) and high-resolution TEM (HRTEM) were employed to further characterize the structure of the $CdS/Cu_2O/Fe_2O_3$ sample, as shown in Figure 30. From the TEM picture, there are some small particles on the surface of Fe_2O_3. From the HRTEM picture, the lattice fringes of the CdS and Cu_2O, which were measured to be 0.245 nm and 0.142 nm, corresponding to (102) and (221) facet of each, respectively. It is clear to identify that CdO nanoparticles deposited on the surface of Fe_2O_3 and coated with Cu_2O nanoparticle. From the HRTEM pattern,

the Cu_2O seems to selectively deposit on the CdS. Cu^{2+} tend to adsorb on the surface of CdS, as the electronic structure, atomic size and precursor of Cu^{2+} is close to the Cd^{2+}.

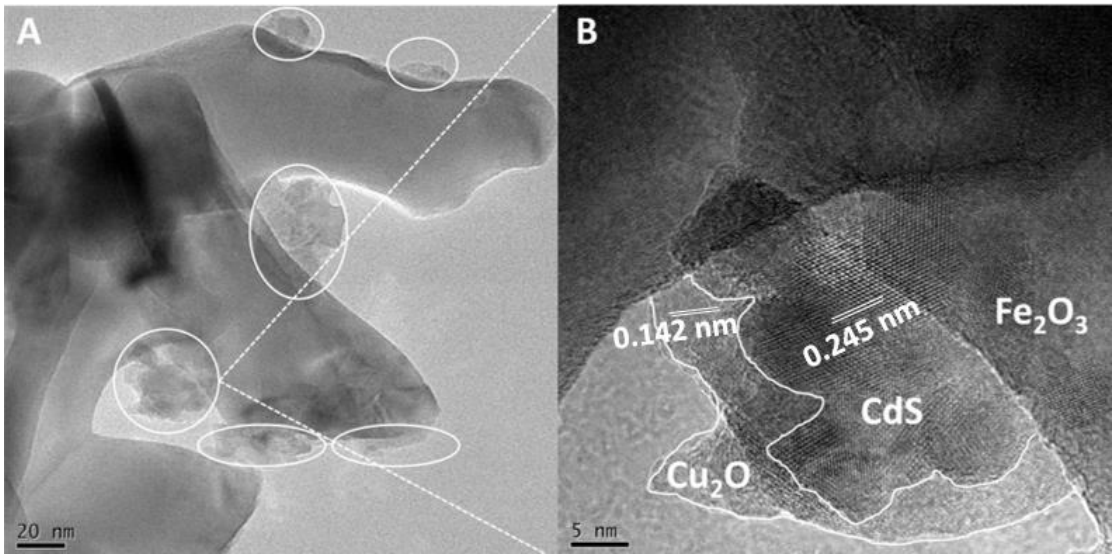

Figure 30: The (A) TEM and (B) HRTEM of $Cu_2O/CdS/Fe_2O_3$.

3.3.4: Chemical state characterisation

XPS was performed to characterize the chemical state of Fe_2O_3 and $Cu_2O/CdS/Fe_2O_3$. Figure 31A shows the Fe *2p* pattern of Fe_2O_3 and $Cu_2O/CdS/Fe_2O_3$. The $2p_{3/2}$ and $2p_{1/2}$ core levels of Fe species are discerned at around 710.7 and 724.1 eV, respectively. There is no doubt that the Fe is +3 oxidation state in Fe_2O_3.[46]

The chemical state of O in the Fe_2O_3 and $Cu_2O/CdS/Fe_2O_3$ was showed in Figure 31B. For Fe_2O_3, there are two kinds of O atom. The lower energy peak, around 529.6 eV, could be attributed to the lattice O-Fe, and the higher energy peak, around 531.5 eV, presents the hydroxyl oxygen and adsorbed oxygen on the surface of Fe_2O_3.[46] For $Cu_2O/CdS/Fe_2O_3$, the peak which belongs to adsorbed OH group remains at the same position as Fe_2O_3. But, there are two kinds of crystal lattice oxygen. The peak around 529.6 eV can be attributed to the O-Fe also. According to some literatures, the peak around 530.2 belongs to the lattice oxygen in Cu_2O.[99]

Two S*2p* binding energy peaks are discerned at around 161.5 and 168.9 eV which corespond to different chemical environments of sulfur atoms in the CdS lattice. The lower BE S*2p* at 161.5 eV is in good agreement with the literature values, indicating that the valence states of S is −2.[100, 101] The higher BE S*2p* signatures around 169 eV have been previously assigned to S^{4+} species located at the edges of CdS layers.[101] The signal is composed of two overlapping peaks, 169.5 and 168.5, which correspond to the $2p_{1/2}$ and $3d_{3/2}$. It indicates that the CdS is in good contact with the Cu_2O and Fe_2O_3. As shown in Figure 31D, there is no doubt that the valence state of Cd is +2. The peaks of $Cd3d_{5/2}$ and $Cd3d_{3/2}$ are around 405.2 eV and 412.0 eV, respectively.[100]

Two signals ascribed to $2p_{3/2}$ and $2p_{1/2}$ core levels of Cu species are discerned at around 932.5 and 952.50 eV, respectively. This shows that Cu is in the +1 oxidation state in the $Cu_2O/CdS/Fe_2O_3$ sample.[102, 103]

The effect of Cu_2O and CdS on the Fe_2O_3 valence band (VB) was explored by comparison of the VB-XPS spectra of Fe_2O_3 and $Cu_2O/CdS/Fe_2O_3$, as shown in Figure 31F. A significant upward shift of the O*2p*-VB edge of Fe_2O_3 was observed after being decorated with Cu_2O and CdS which weakens the oxidizing power. This could be attributed to the VB of Cu_2O and CdS which are at a lower potential than Fe_2O_3.

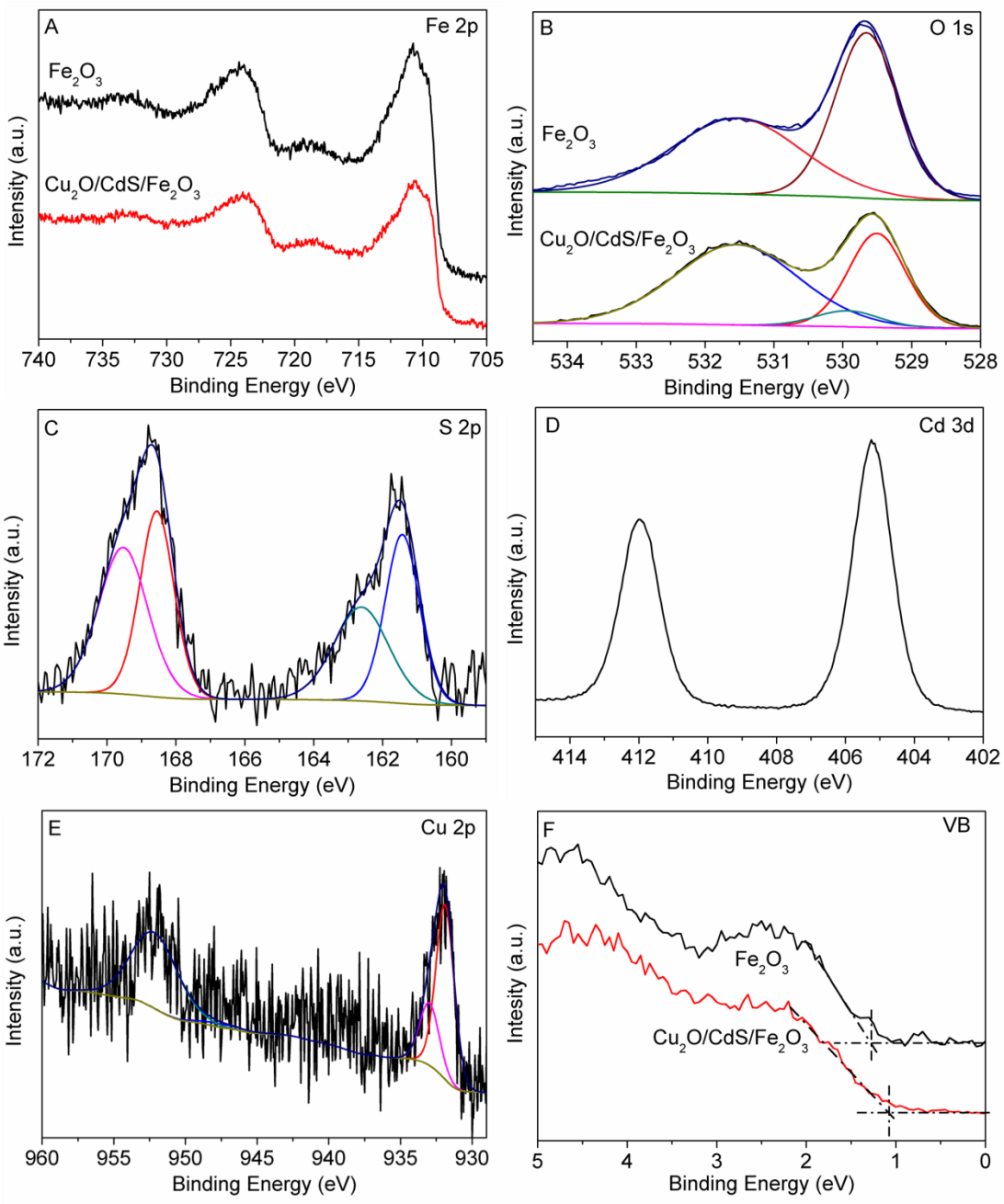

Figure 31: The high-resolution core XPS spectra of (A)Fe2p and (B)O1s of Fe_2O_3 and $Cu_2O/CdS/Fe_2O_3$ samples, (C)S2p, (D)Cd3d and (E)Cu2p of $Cu_2O/CdS/Fe_2O_3$ samples and (F)Valence band of Fe_2O_3 and $Cu_2O/CdS/Fe_2O_3$ samples.

3.3.5: UV-vis spectroscopy

The UV-vis transmission spectrum of Fe_2O_3, CdS/Fe_2O_3, Cu_2O/Fe_2O_3 and $Cu_2O/CdS/Fe_2O_3$ is shown in Figure 32. The band-edge absorption of Fe_2O_3 is around 570 nm which is corresponding to the band-gap of Fe_2O_3 (2.3 eV).[44] It is easy to

observe a weak red shift of band-edge absorption and absorption tail enhanced in visible light area, after coating with CdS. However, the Cu_2O coating causes a blue shift on band-edge of Fe_2O_3 and the absorption tail decreases. Interestingly, coupled with CdS and Cu_2O, there is a significant absorption increase in the composite film. It could be attributed to the increase of surface oxygen defect, which could increase the Urbach Tail absorption. Oxygen atoms in the interface between Fe_2O_3 and CdS and Cu_2O and CdS could bind with S atoms, which is in accordance with the XPS result of S*2p*.

.

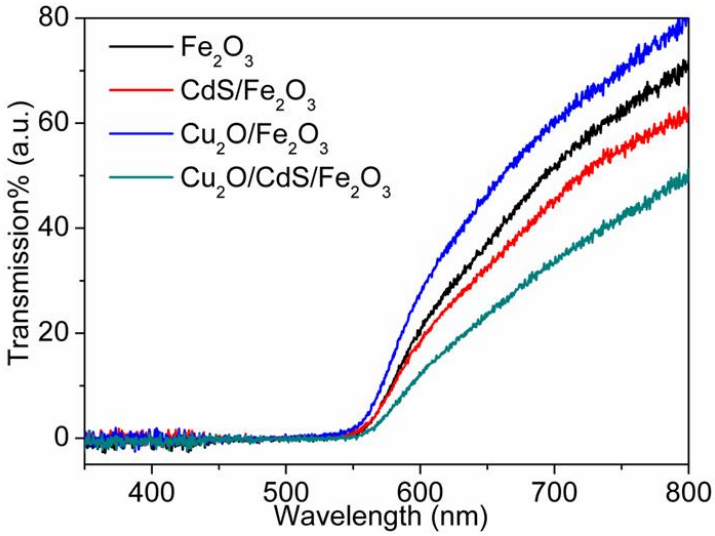

Figure 32: The UV-vis transmission spectrum of Fe_2O_3 CdS/Fe_2O_3, Cu_2O/Fe_2O_3 and Cu_2O/CdS/Fe_2O_3 samples.

3.3.6: Photoelectrochemical Performance for Water Oxidation

PEC measurements were carried out in a three-electrode system, with the Fe_2O_3 based nanorod arrays as the working electrode, a Pt foil as the counter electrode, Ag/AgCl as a reference electrode, and the NaOH electrolyte (1 M).

The photocurrent density versus applied voltage scans of the samples were measured under AM 1.5G simulated sunlight (100 mW/cm^2). As shown in Figure 33, under light irradiation, the photocurrent density of Cu_2O/CdS/Fe_2O_3 which could reach at 1.6 mA/cm^2 at 1.23 V vs RHE was significantly enhance, as compared to Fe_2O_3.

With the same bias, Fe_2O_3 yielded a photocurrent density of 1.2 mA/cm^2. Interestingly, compared with Fe_2O_3, the photocurrent density of CdS/Fe_2O_3 and Cu_2O/Fe_2O_3 show a lower value which is 0.15 and 0.6 mA/cm^2, respectively.

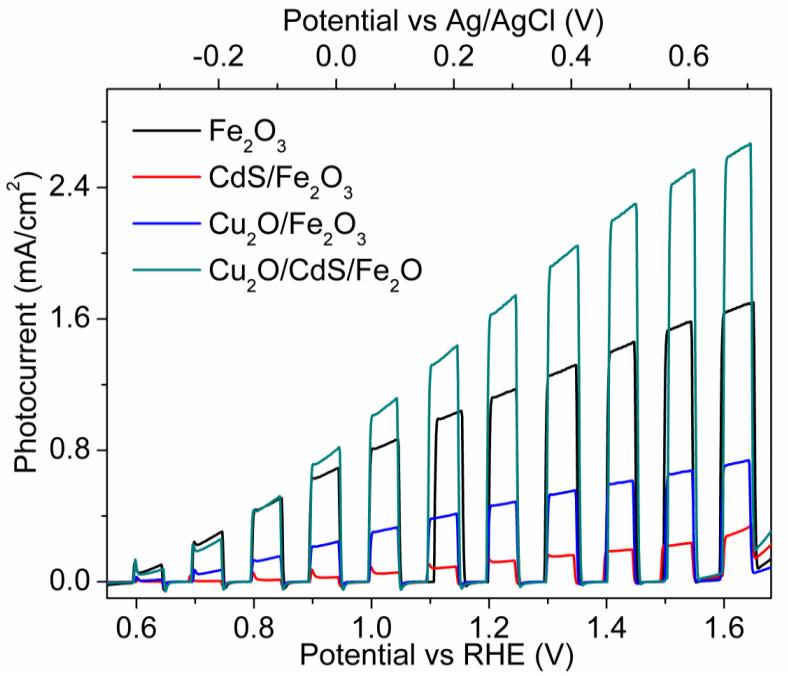

Figure 33: Current density-potential (j-E) curves of Fe_2O_3 CdS/Fe_2O_3, Cu_2O/Fe_2O_3 and $Cu_2O/CdS/Fe_2O_3$ under 1-sun light illumination

For CdS/Fe_2O_3, the lower photocurrent density could be attributed to the oxidation of CdS.[104] As some publications described, the valence band of Cu_2O which is 1.3 V vs RHE is close to the conduction band of Fe_2O_3 which is 0.4 V vs RHE, and the conduction band of Cu_2O is -0.7 V.[97, 105] The holes generated on the valence band of Fe_2O_3 could not move to Cu_2O. But the recombination happens between electrons generated by Fe_2O_3 and holes on the Cu_2O.[105] For the $Cu_2O/CdS/Fe_2O_3$ photoanode, the CdS layer could act as a step that the holes generated on Fe_2O_3 could transfer to Cu_2O, and a barrier to block the carries recombination between Fe_2O_3 and Cu_2O. At the same time, Cu_2O could extract hole from CdS layer which could inhibit the self-oxidized of CdS, as shown in Figure 34. Alternatively the interfaces between oxide and sulphide materials support more rapid charge transfer in comparison to an oxide-oxide interface present in Fe_2O_3/Cu_2O.

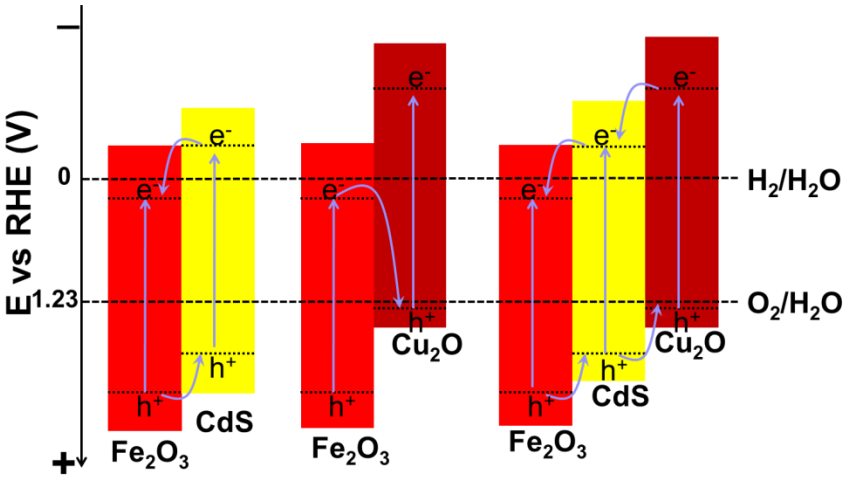

Figure 34: the energy level of CB and VB in the CdS/Fe_2O_3, Cu_2O/Fe_2O_3 and $Cu_2O/CdS/Fe_2O_3$

The on/off photocurrent density response under 1-sun irradiation is consistent with the result obtained from the LSV spectrum. The on/off photocurrents were tested in 1 M NaOH and 1.23 V vs RHE, which is also shown in Figure 35A. The composite $Cu_2O/CdS/Fe_2O_3$ exhibits the best photocurrent density among all samples. Although there is a heterojunction between Cu_2O and Fe_2O_3, the current of Cu_2O/Fe_2O_3 is lower than the pure Fe_2O_3 which confirms the aforementioned results. The current decreases in the order $Cu_2O/CdS/Fe_2O_3$ > Fe_2O_3 > Cu_2O/Fe_2O_3 > CdS/Fe_2O_3. The stability performance of all samples was shown in Figure 35B. $Cu_2O/CdS/Fe_2O_3$, Fe_2O_3 and Cu_2O/Fe_2O_3 show substantially stable performance. However, a decrease could be observed from CdS/Fe_2O_3 if we enlarge the stable performance curve which was show in Figure 35C. It is obvious that about 30% decrease happened after 5 mins irradiation. After covered with Cu_2O on the CdS, the current keeps stable for a long time indicating that the self-oxidation of CdS was suppressed.

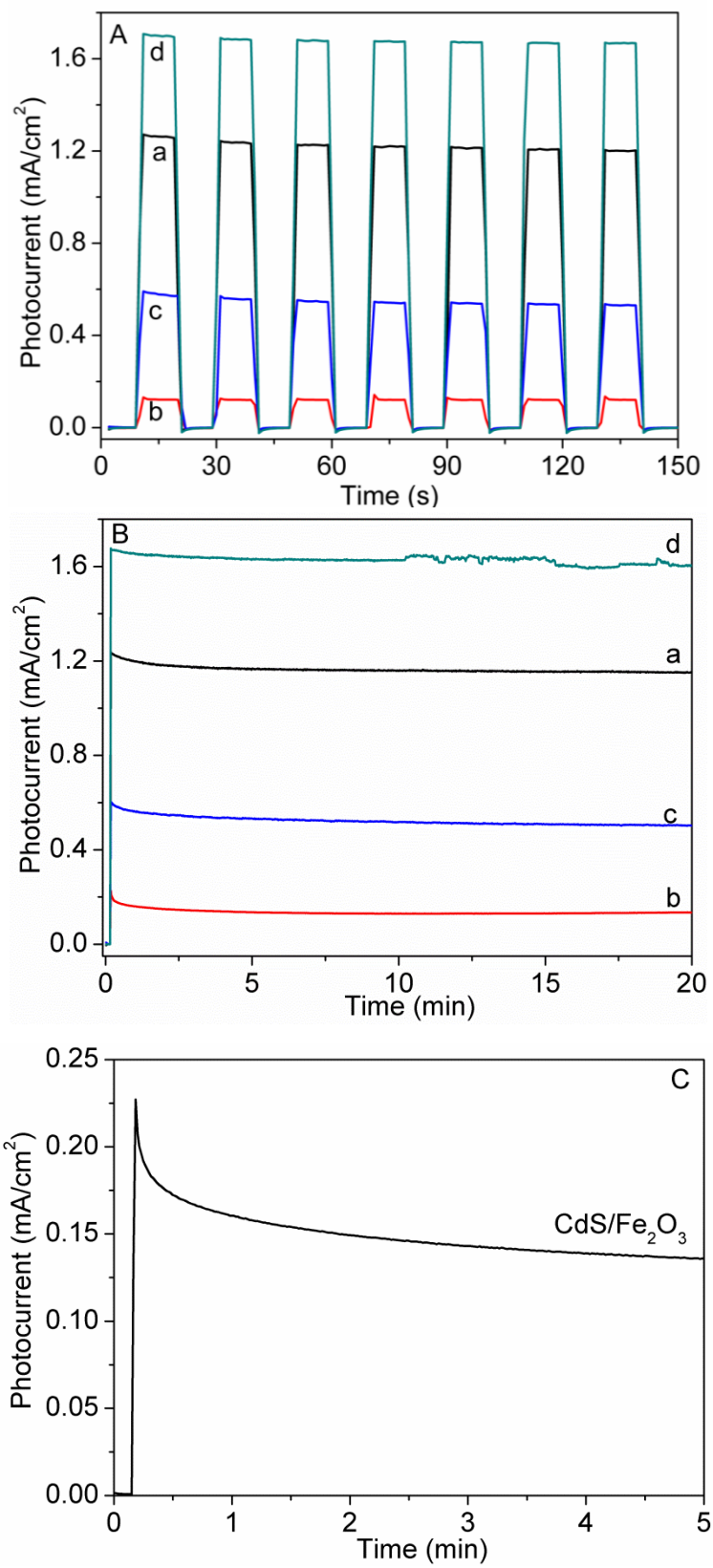

Figure 35: (A)The periodic on/off photocurrent response, (B) stable performance of Fe_2O_3 (a), CdS/Fe_2O_3 (b), Cu_2O/Fe_2O_3 (c) and $Cu_2O/CdS/Fe_2O_3$ (d) and (C) 5 mins stable performance of CdS/Fe_2O_3 at 1.23V vs RHE under sun light irradiation.

3.3.7: Impedance characteristics

To further understand the enhanced photocurrent density and stability of the ternary composite photoanode, we conducted a Mott-Schottky analysis and EIS measurements for the Fe_2O_3, CdS/Fe_2O_3, Cu_2O/Fe_2O_3 and $Cu_2O/CdS/Fe_2O_3$.

Figure 36 shows the Mott-Schottky (M-S) plot for all hematite thin films recorded under dark conditions. All hematite thin films are typical n-type semiconductor based on the positive slope of all samples in the M-S spectrum.[106, 107, 108] According to the slope and intercept of these plots in the M-S spectrum, the donor densities (N_D) and flat band potential (FB) of the Fe_2O_3, CdS/Fe_2O_3, Cu_2O/Fe_2O_3 and $Cu_2O/CdS/Fe_2O_3$ electrodes could be compared (Table 3). From the slope, the conclusion could be made that the donor density decreases in the order of $Cu_2O/CdS/Fe_2O_3$ > CdS/Fe_2O_3 Cu_2O/Fe_2O_3 > Fe_2O_3.[109, 110]

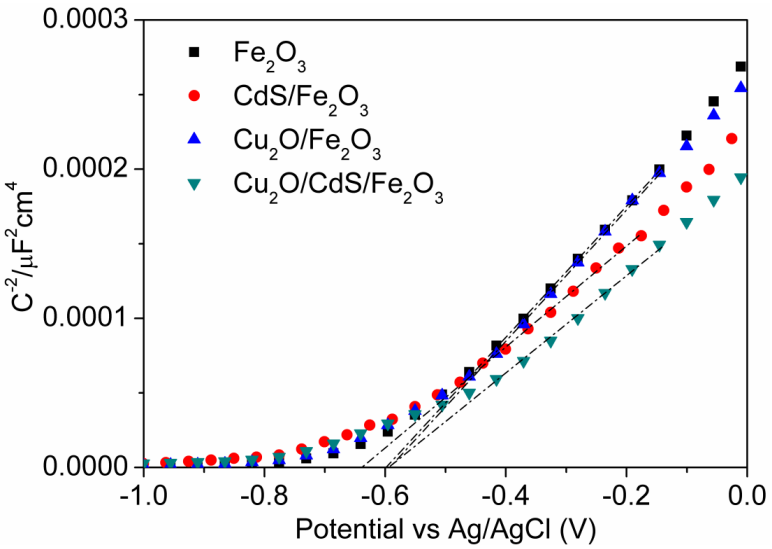

Figure 36: The Mott-Schottky plots of Fe_2O_3, CdS/Fe_2O_3, Cu_2O/Fe_2O_3 and $Cu_2O/CdS/Fe_2O_3$.

Table 3: Mott–Schottky parameters of Fe_2O_3, CdS/Fe_2O_3, Cu_2O/Fe_2O_3 and $Cu_2O/CdS/Fe_2O_3$.

Sample	Flat Potential (V vs Ag/AgCl)	Donor Density x 10^{19} (cm^{-3})
Fe_2O_3	-0.60	15.30
CdS/Fe_2O_3	-0.64	20.78
Cu_2O/Fe_2O_3	-0.59	16.55
$Cu_2O/CdS/Fe_2O_3$	-0.59	22.95

To gain further insight into the enhanced photocurrent and stability mechanism of $Cu_2O/CdS/Fe_2O_3$, the Nyquist plots of Fe_2O_3, CdS/Fe_2O_3, Cu_2O/Fe_2O_3 and $Cu_2O/CdS/Fe_2O_3$ were measured under 1-sun light illumination as shown in Figure 37. In the Nyquist plot, the radius of the arc is associated with the charge-transfer resistance, a smaller radius is correlated with a lower charge-transfer resistance.[46, 111] Cu_2O/Fe_2O_3 shows the largest radius followed by CdS/Fe_2O_3, and both of them are bigger than Fe_2O_3, which is consistent with the photocurrent density. For Cu_2O/Fe_2O_3, the holes generated on the VB of Fe_2O_3 could not transfer to Cu_2O, due to energy mismatch as shown in Figure 34.[105] Although the energy of VB and CB of CdS and Fe_2O_3 are beneficial for the carrier transportation, CdS is not a good catalyst for water oxidation because the sulfide is oxidized corroding the electrode. The oxidation of CdS would suppress hole transfer and could enhance the resistance in the interface between electrode and electrolyte.[104] Interestingly, $Cu_2O/CdS/Fe_2O_3$ showed a smaller radius than that of other electrodes which suggests that an effective separation of photo-generated electron–hole pairs and faster interfacial charge transfer occurs. It means that CdS could act as a hole transfer pathway so that the holes generated in the VB of Fe_2O_3 could transfer to the Cu_2O. As the holes transfer to Cu_2O, the oxidation of CdS decreases.

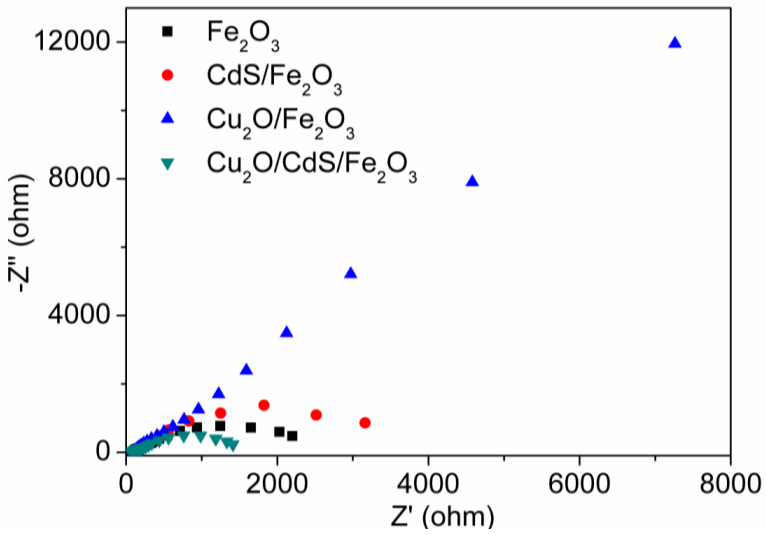

Figure 37: Nyquist plots of Fe_2O_3, CdS/Fe_2O_3, Cu_2O/Fe_2O_3 and $Cu_2O/CdS/Fe_2O_3$. The EIS spectra were measured in 1.0 M NaOH at 1.23 V vs RHE under 1-sun light irradiation.

3.3.8: IPCE measurements

The incident photon-to-current efficiencies (IPCE) of the Fe_2O_3, CdS/Fe_2O_3, Cu_2O/Fe_2O_3 and $Cu_2O/CdS/Fe_2O_3$ photoanodes have been measured under monochromatic light irradiation and plotted as a function of wavelength at 1.23 V vs RHE.

The IPCEs for all samples showed the same tendency. The IPCE drops sharply as the wavelength increases. The $Cu_2O/CdS/Fe_2O_3$ photoanode shows the highest efficiency which was measured to be above 10 % for the incident light wavelength shorter than 450 nm. Then, the IPCE of Fe_2O_3 is better than CdS/Fe_2O_3 and Cu_2O/Fe_2O_3, which confirms the aforementioned results that we obtained from EIS and PEC test.

Thus, this result demonstrates that the co-modification of the Cu_2O and CdS nanoparticles can accelerate the water splitting reaction and improve the charge transfer processes.

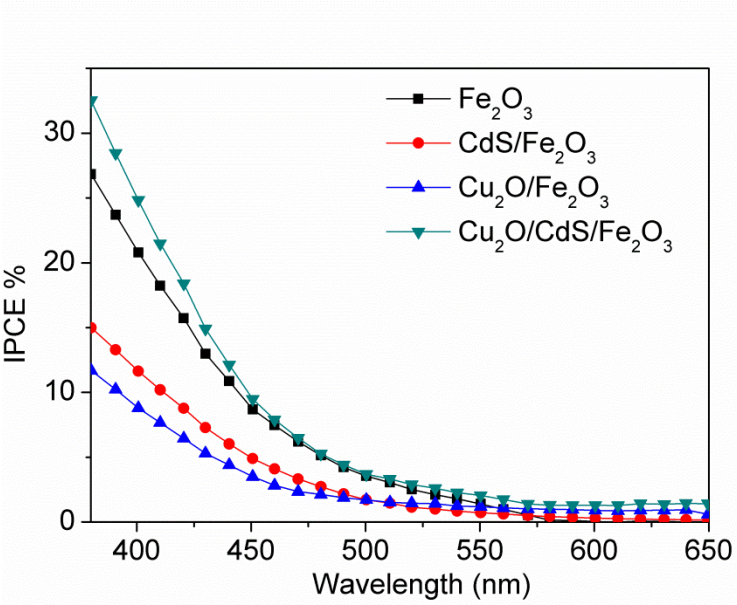

Figure 38: IPCE performance of Fe_2O_3 CdS/Fe_2O_3, Cu_2O/Fe_2O_3 and $Cu_2O/CdS/Fe_2O_3$ at 1.23V vs RHE.

3.4: Conclusion

In this chapter, we reported that the CdS/Fe_2O_3 could be used as photoande if the self-oxidation of CdS could be inhibited by heterojunction formation. In this $Cu_2O/CdS/Fe_2O_3$ photoanode, the coupling of Cu_2O, CdS and Fe_2O_3 not only supports stepwise charge transfer between Cu_2O and Fe_2O_3 to achieve the hole transfer from Fe_2O_3 to Cu_2O, but also inhibits CdS oxidation. The $Cu_2O/CdS/Fe_2O_3$ photoanode exhibited enhanced PEC water oxidation performance and high stability. In summary, this work offers a guide to design novel photoanode with ternary heterojucntions to achieve higher efficiency and stability for solar energy conversion.

Chapter 4

Photochemical route for depositing amorphous cobalt oxide as a water oxidation catalyst on Fe_2O_3 photoelectrodes

4.1 Introduction

In this chapter, a new type of Co based cocatalyst was introduced and used to decorate Fe_2O_3 photoanode to improve the charge carrier transfer and enhance the OER activity.

Co based cocatalyst for water oxidation has been discussed in many publications. Some Co oxide crystalline materials exhibit good water oxidation activity.[89] In recent years, amorphous metal oxides have also been demonstrated to be excellent OER catalysts.[112] Electrodeposited Co-Pi is a typical amorphous catalyst (OER) and the most popular catalyst since it was found by Diane K. Zhong and co-workers.[61] M. Gratzel and his co-workers found that photo-assisted electrodeposition of Co-Pi could further improve the water oxidation, compared with electrodeposited Co-Pi.[113] But electrodeposition techniques are limited by the voltage protocol, and the composites of deposition are unknown and not homogeneous.[112] Hereby, we report a UV light deposited amorphous Co oxide on Fe_2O_3 films which could show a better activity compared with Fe_2O_3 nanoparticles.

4.2: Chapter aims

The aim of this chapter is to present a new method to deposit amorphous CoO_x as a cocatalyst on Fe_2O_3 surface to improve the O_2 release from water.

In this chapter, the synthesis and characterization of CoO_x/Fe_2O_3 photoanode will be presented. In comparison with the Fe_2O_3, an enhancement of the photocurrent density has been observed on the CoO_x/Fe_2O_3 photoanode. Like some published Co based cocatalyst, Co-Pi and Co_3O_4, amorphous CoO_x excels at water oxidation.

All of the as-prepared samples were characterized in detail by X-ray diffraction (XRD),

Scanning Electron Microscopy (SEM), Transmission Electron Microscopy (TEM), X-ray photoelectron spectroscopy (XPS), UV-Vis Transmittance Spectroscopy, Photoelectrochemistry (PEC), Electrochemical Impendence Spectroscopy (EIS) and Incident-Photon-to-Current-Efficiency Measurement (IPCE).

4.3: Result and discussion

4.3.1: Synthesis of amorphous CoO_x/Fe_2O_3 nanorod arrays

The Fe_2O_3 nanorod arrays were prepared by a modified literature report.[76] A FTO glass (1 cm × 3 cm) was placed in hydrothermal reactor, with aqueous $FeCl_3$. The reaction was heated at 100 °C for 6 h and after cooling rinsed with deionized water and annealed in air at 550 °C for 2 h and 800 °C for 20 min. The amorphous CoOx coating on the surface of Fe_2O_3 was prepared by a modified literature report.[112] Cobalt 2-ethylhexanoate was diluted into 0.5 mM by hexane. Fe_2O_3 films were dipped into the 0.5 mM cobalt 2-ethylhexanoate hexane solution for 0.5 min, 1 min, 2 min, 5 min and 10 min, and then irradiated with UV light for 6 h, and heated at 100 ^oC for 1 h. These samples were identified as 0.5-CoO_x/Fe_2O_3, 1-CoO_x/Fe_2O_3, 2-CoO_x/Fe_2O_3, 5-CoO_x/Fe_2O_3 and 10-CoO_x/Fe_2O_3, respectively.

4.3.2: Structural and morphology characteristics

Figure 39 shows the XRD pattern of Fe_2O_3 and 2-CoO_x/Fe_2O_3. From the XRD pattern, the peaks belong to Fe_2O_3 and FTO.[63] No diffraction peaks, except (110), arising from iron oxides are observed in the XRD patterns of both samples which means that the Fe_2O_3 nanorods were prepared successfully.[63] XRD revealed no evidence for a crystalline phase of cobalt oxide, indicating that the cobalt oxide is amorphous and does not change the structure of Fe_2O_3.[114]

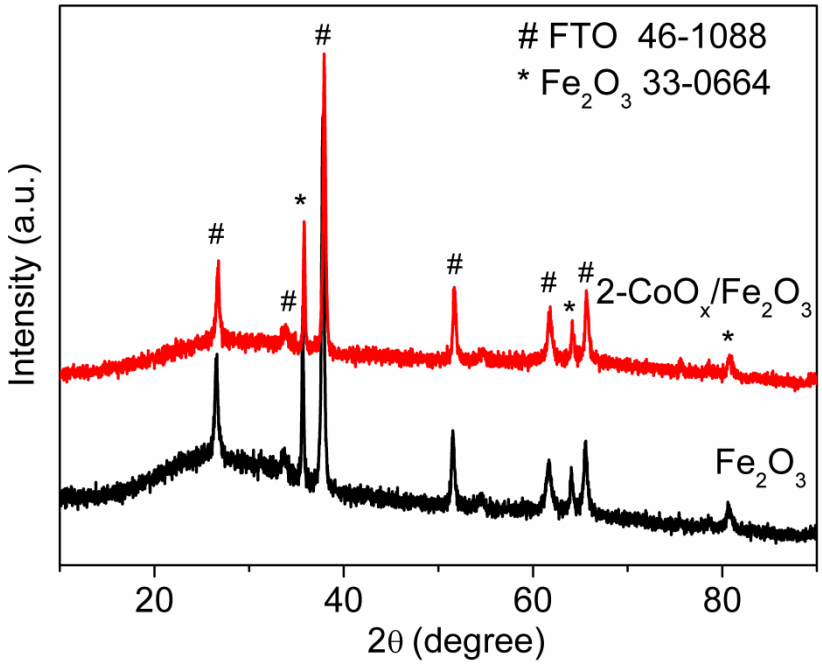

Figure 39: The XRD patterns of as-prepared Fe_2O_3 and 2-CoO_x/Fe_2O_3 samples.

These results could be further confirmed by SEM and TEM. The SEM pictures of Fe_2O_3 and 2-CoO_x/Fe_2O_3 are shown in Figure 40. Based on the top-view pictures, the rod shape of Fe_2O_3 was identified which is consistent to the XRD result.[60, 76] In comparison to bare Fe_2O_3, 2-CoO_x/Fe_2O_3 still showed a rod structure and no obvious difference could be observed.

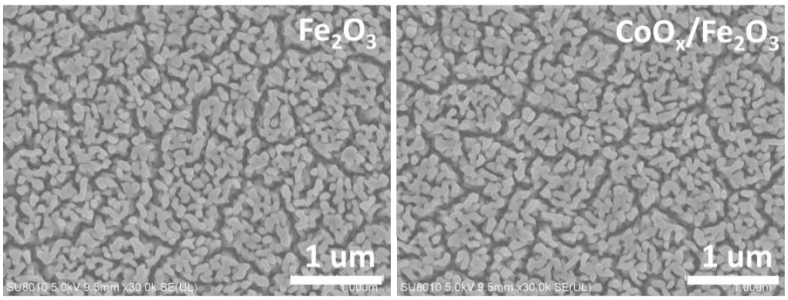

Figure 40: Scanning electron micrographs of the top view of the Fe_2O_3 and CoO_x/Fe_2O_3

The TEM and HRTEM pictures of CoO_x/Fe_2O_3 and Fe_2O_3 are shown in Figure 41. From the TEM picture, the nanorod structure of CoO_x/Fe_2O_3 and Fe_2O_3 could be confirmed and the diameter of the nanorods is ca. 50 nm. Compared with the TEM

images of the CoO_x/Fe_2O_3 and Fe_2O_3, some small particles at the edges of the Fe_2O_3 rod could be found in 2-CoO_x/Fe_2O_3, as shown in Figure 36. The HRTEM images of both samples give only one lattice fringe with an interplanar space of about 0.25 nm, which is indexed as the d_{110} spacing of □-Fe_2O_3.[115] However, no lattice fringes of cobalt oxide species could be observed in 2-CoO_x/Fe_2O_3, implying that amorphous CoO_x nanoparticles formed on the surface of Fe_2O_3.

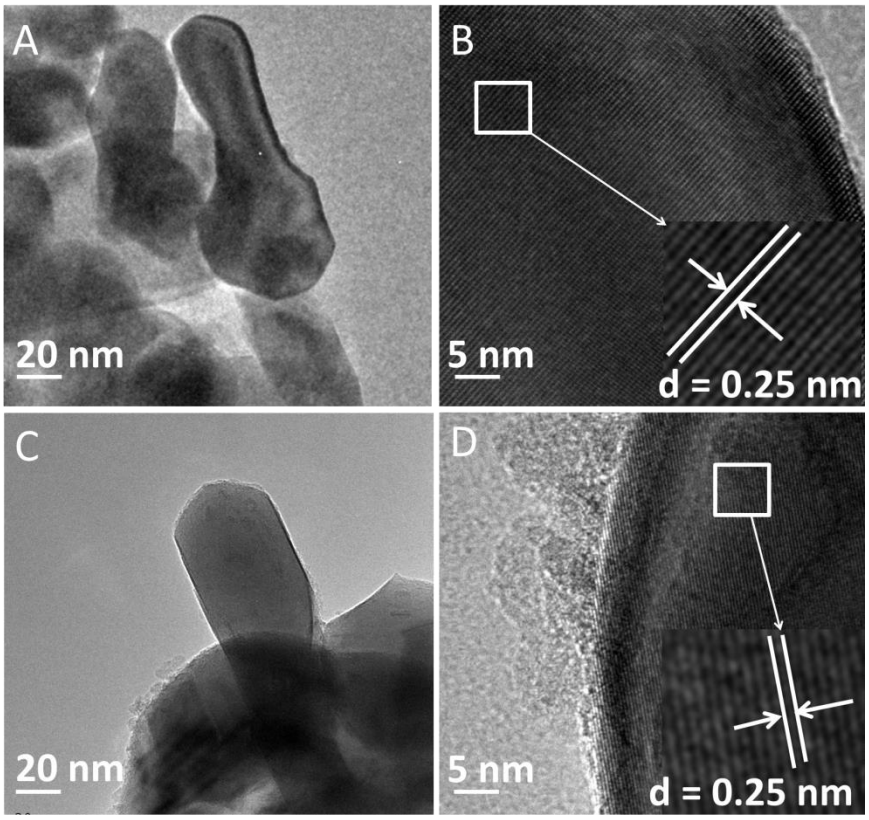

Figure 41: TEM and HRTEM images of Fe_2O_3 (A and B) and CoO_x/Fe_2O_3 (C and D) The insets to (B) and (D) show the corresponding interplanar space.

4.3.3: UV-vis spectroscopy

The UV-vis spectrum of Fe_2O_3 and CoO_x/Fe_2O_3 are shown in Figure 42. The bare Fe_2O_3 nanorod shows the band-edge absorption at approximately 560 nm which is corresponding to a 2.1 eV band-gap.[44] After coating with a thin layer of CoO_x, the band-edge absorption shifts to a shorter wavelength. However, CoO_x/Fe_2O_3 showed a

stronger absorption tail in the visible light region, compared with Fe_2O_3, possibly owing to the defects in the surface layer which will increase the Urbach Tail.[80, 82] It may be caused by the amorphous of CoO_x layer containing lots of defects which are in agreement with the results of XRD and TEM.[116]

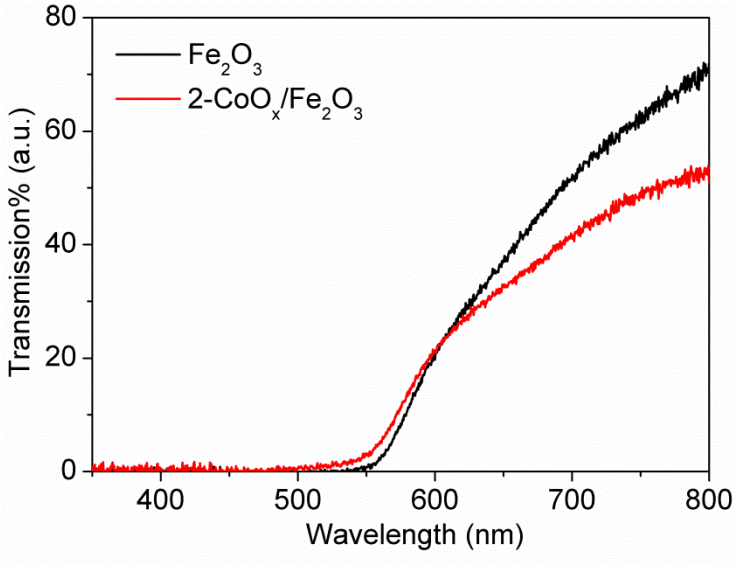

Figure 42: The UV-vis transimission spectra of Fe_2O_3 and CoO_x/Fe_2O_3.

4.3.4: Chemical States characteristics

XPS was performed to characterize the chemical states of amorphous CoO_x coating on Fe_2O_3. The XPS spectra of parent Fe_2O_3 and CoO_x/Fe_2O_3 are shown in Figure 43.

.

In Fe2p XPS spectra, two main peaks assigned to $2p_{3/2}$ and $2p_{1/2}$ core levels of Fe species are discerned at around 710.7 and 724.8 eV, respectively. Between these two peaks, a peak around 719.0 eV which is located approximately 8 eV higher than the main Fe $2p_{3/2}$ peak is the satellite peak of Fe $2p_{3/2}$.[46] In comparison to Fe_2O_3 with CoO_x/Fe_2O_3, no change is observed in the position of Fe 2p peaks, but the peak intensity of Fe 2p in CoO_x/Fe_2O_3 was weaker than Fe_2O_3, indicating a thin layer covers the Fe_2O_3 which does not change the valence state of Fe.

The O1s binding energy spectra obviously demonstrate two peaks in the region from 528.0 eV to 534 eV, indicating that more than two forms of oxygen chemical states exists in the compounds. For the curve of Fe_2O_3, the peak at 529.6 and 531.6 eV could be attributed to O in the Fe_2O_3 crystal lattice and hydroxyl oxygen and adsorbed oxygen on the surface of Fe_2O_3, respectively.[46] The intensity belonging to O in the Fe_2O_3 crystal lattice is stronger than adsorbed hydroxyl oxygen. However, CoO_x coating Fe_2O_3 showed a stronger peak around 531.6 eV which could be attributed to off-lattice O structure and a weaker one around 529.3 eV which could be attributed to Fe-O in Fe_2O_3, indicating an amorphous structure on the surface which further confirm the result obtained from TEM and XRD.

The Co chemical state in CoO_x was measured by XPS. It is easy to identify two main peaks around 779.8 and 795.6 eV which could be assigned to $2p_{3/2}$ and $2p_{1/2}$ core levels of Co species, respectively. Through deconvolution of Co $2p_{3/2}$, the spectra shows that the Co species exist with +2 and +3 oxidation states.[72, 117, 118] However, the ratio between Co^{+3} and Co^{+2} was close to 1:1 rather than 2:1, indicating that the deposited CoO_x layer is not CoO or Co_3O_4.

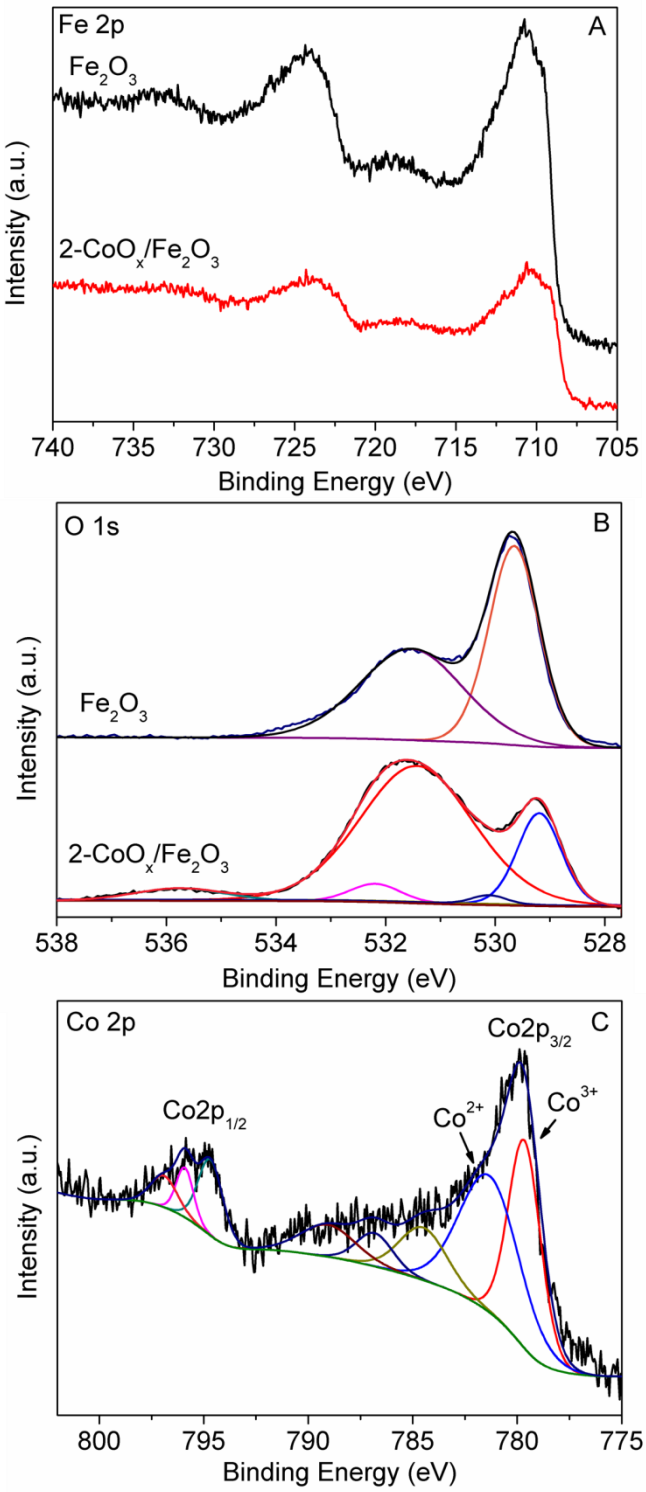

Figure 43: The high-resolution core XPS spectra of (A)Fe2p and (B)O1s of Fe_2O_3 and CoO_x/ Fe_2O_3 samples, (C)Co2p of CoO_x/ Fe_2O_3 sample.

4.3.5: Photoelectrochemical Performance for Water Oxidation

The PEC performance of photoanode was obtained in 1 M NaOH electrolyte 1-Sun light irradiation (AM1.5 G, 100 mW/cm^2). The measured potentials vs Ag/AgCl were converted to the reversible hydrogen electrode (RHE) scale according to the Nernst equation. The current–voltage (J–V) characteristics of representative Fe_2O_3 and CoO_x/Fe_2O_3 photoelectrodes are shown in Figure 44A. It was found that CoO_x layer gave rise to a strong effect on the photocurrent–potential characteristics. At 1.23 V vs RHE, the photocurrent density increased as the dip time increased from 0.5, 1 and 2 mins, respectively. The enhancement of the photocurrent can be attributed to the catalytic effect of the CoO_x layer and photo absorption increased due to the defects on CoO_x layer. After 5 mins and 10 mins dipped, the photocurrent density decrease, which was probably due to the formation of thick CoO_x layer on the surface of hematite nanorods, which may block the hole transport to the interface. Form Figure 44B, the photocurrent density of 2-CoO_x/Fe_2O_3, which is 1.5 mA/cm^2, increase by 1.5 times compared with bare Fe_2O_3 which is 0.6 mA/cm^2. In 2010, Zhong and Gamelin prepared Co-Pi/Fe_2O_3 by electrodeposition, the Co-Pi/Fe2O3 presented 0.8 mA/cm^2 under 1 sun, pH 13.6 and 1.23 V vs RHE.[119] In 2011, Zhong and his co-workers prepared Co-Pi/Fe_2O_3 photoanode by photo-assisted electrodeposition method, which showed 0.5 times enhanced compared with bare Fe_2O_3.[113]

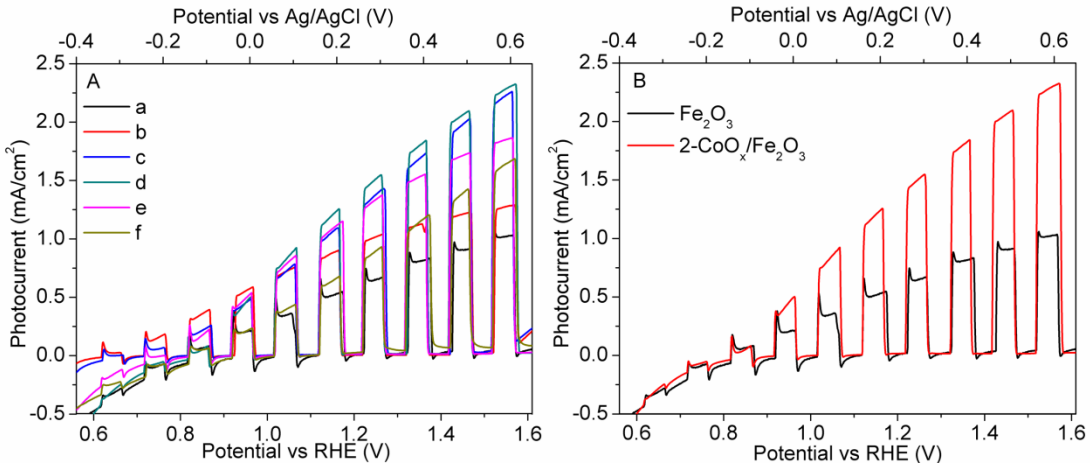

Figure 44: (A) Current density-potential (J-V) curves of Fe_2O_3 (a), 0.5-CoO_x/Fe_2O_3 (b),

1-CoO_x/Fe_2O_3 (c), 2-CoO_x/Fe_2O_3 (d), 5-CoO_x/Fe_2O_3 (e) and 10-CoO_x/Fe_2O_3 (f) under sun light illumination and (B) Current density-potential (J-V) curves of Fe_2O_3 and 2-CoO_x/Fe_2O_3 under sun light illumination

The on/off photocurrent response under sun light, is also shown in Figure 45A. The photocurrent intensity at 1.23 V vs RHE decreases in the order of 2-CoO_x /Fe_2O_3 > 1-CoO_x /Fe_2O_3> 0.5-CoO_x /Fe_2O_3 > 5-CoO_x /Fe_2O_3 > 10-CoO_x/Fe_2O_3 > Fe_2O_3 under 1-Sun light irradiation. All photoanodes show substantially stable performance, as shown in Figure 45B. There is no obvious decline after 20 min irradiation.

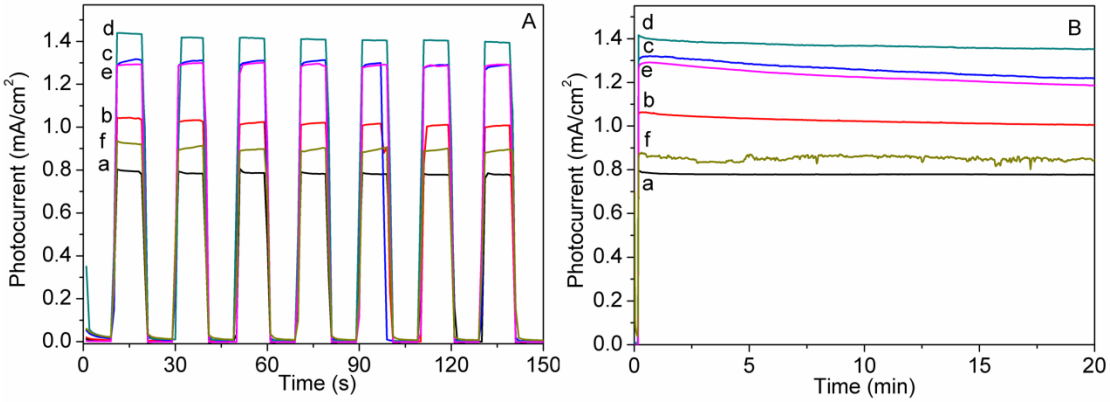

Figure 45: (A)The periodic on/off photocurrent response and (B) stable performance of Fe_2O_3 (a), 0.5-CoO_x/Fe_2O_3 (b), 1-CoO_x/Fe_2O_3 (c), 2-CoO_x/Fe_2O_3 (d), 5-CoO_x/Fe_2O_3 (e) and 10-CoO_x/Fe_2O_3 (f) at 1.23V vs RHE under sun light irradiation.

4.3.6: Impedance characteristics

To study the reason of photocurrent density increase by CoO_x layer coating, the electrochemical impedance spectroscopy (EIS) was measured.

Figure 46 displays the Mott-Schottky (M-S) plot for all hematite thin films recorded under dark condition. The donor densities and flat band potential of the Fe_2O_3 and 2-CoO_x/Fe_2O_3 electrodes have been obtained from the slope of these plots based on the M-S equation, as shown in Table 4. After CoO_x coating, the flat-band potential almost keeps the same position compared with bare Fe_2O_3. This result is consistent

with the photocurrent–potential data, the same on-set potential was observed for the sample with 2-CoO_x/Fe_2O_3 and pristine hematite. N_D value analysis shows the donor density increases on CoO_x coating and Fe_2O_3 shows the lower donor density compared with 2-CoO_x/Fe_2O_3.

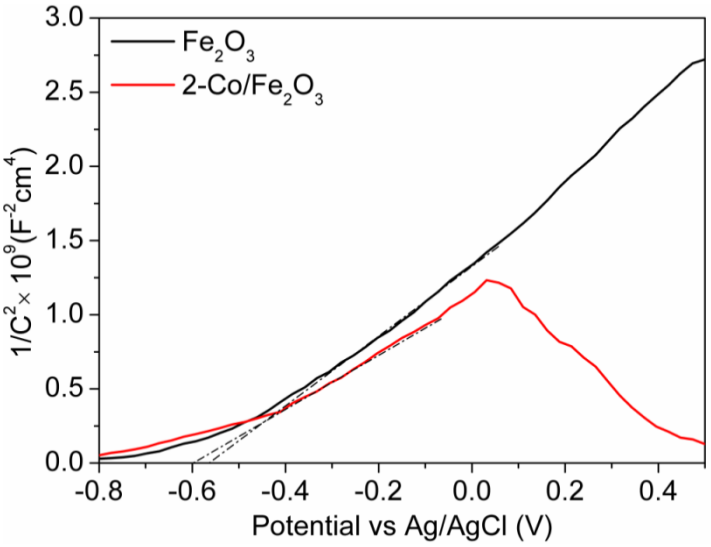

Figure 46: The Mott-Schottky plots of Fe_2O_3 and 2-CoO_x/Fe_2O_3.

Table 4: Mott–Schottky parameters of Fe_2O_3 and 2-CoO_x/Fe_2O_3

Sample	Flat Potential (V vs Ag/AgCl)	Donor Density x 10^{19} (cm^{-3})
Fe_2O_3	-0.598	31.79
2-CoO_x/Fe_2O_3	-0.612	39.12

Fe_2O_3 nanorod synthesized by the method as described above is n-type semiconductor which could be confirmed by the slope of Mott-Schottky curve. Interesting, for 2-CoO_x/Fe_2O_3 sample, an inverted “V-shape” curve at 0.05 V (vs. the Ag/AgCl electrode) could be observed, which are indicative of so-called “p-n junction”.[83] Most cobalt oxide, such as Co_3O_4 and CoO, is a typical n-type semiconductor.[120, 121]. At the same time, we found the Fe_2O_3 nanorod would change to a p-type semiconductor, after UV light irradiated.

To gain further insight into the underlying mechanism, the Nyquist plots of Fe_2O_3 and 2-CoO_x/Fe_2O_3 electrodes were measured at 1.23 V vs RHE and under 1-sun light illumination as shown in Figure 47A. The radius of semicircle corresponds to the resistance of the photoanode.[46, 111] It is easy to obtain the conclusion that the resistance in 2-CoO_x/Fe_2O_3 photoanode is far lower than bare Fe_2O_3 which is further confirmed by the results obtained from photoelectrochemical performance for water oxidation. For more detailed analysis, the experimental EIS data under 1-sun irradiation were fitted into an equivalent circuit model (EC), Figure 48B, using the EIS spectrum analyzer software. The fitted impedance parameter values of the resistances (R) and constant phase elements (CPE) are listed in Table 5. This EC consists of the capacitance of the bulk hematite, C_{bulk}, charge transfer resistance from the valence band of the hematite, R_{trap}, a resistance which is related to the rate of trapping holes in surface states, $R_{ct,trap}$ and the capacitance of surface states, C_{ss}.[111] The R_{trap} and $R_{ct,trap}$ in CoO_x/Fe_2O_3, which is 388 and 105 Ω, respectively, is much less than Fe_2O_3. It indicates that CoO_x coating has benefit for the carrier transfer in bulk and surfaceFe_2O_3. The value of C_{ss} in 2-CoO_x/Fe_2O_3 is 15 times that of Fe_2O_3. The larger C_{ss} means that more holes can be accumulated on the surface states, and it facilitates the participation of holes in the photocurrent conversion processes.[111, 122] These results demonstrate that amorphous CoO_x layer could enhance the charge transfer and separation and is a good catalyst for water oxidation via reduction of recombination.

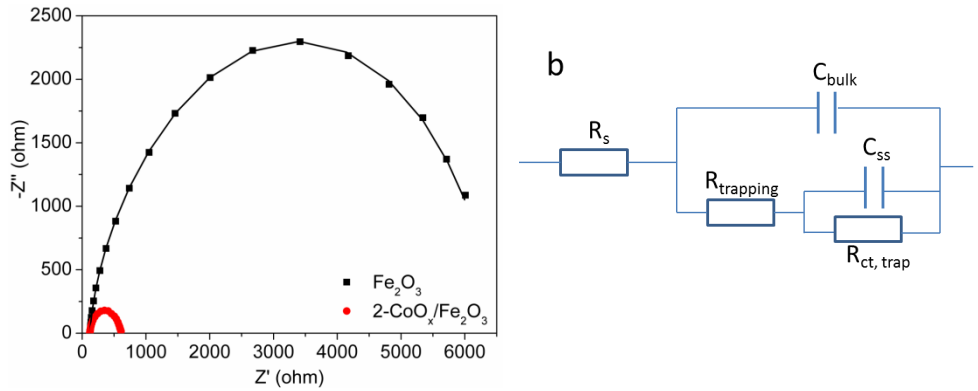

Figure 47: (A) Nyquist plots of Fe_2O_3 and 2-CoO_x/Fe_2O_3 and (B) equivalent circuit model. The EIS spectra were measured in 1.0 M NaOH at 1.23 V vs RHE under sun light irradiation.

Table 5: Resistance and CPE Values Obtained by Fitting the EIS Spectra.

Sample	$R_s(\Omega)$	C_{Bulk} (μF)	$R_{trap}(\Omega)$	C_{ss} (μF)	$R_{ct,trap}$ (Ω)
Fe_2O_3	108	25.56	2778	66.42	3656
2-CoO_x/Fe_2O_3	119	43.74	388	859.5	105

4.3.7: Incident-Photon-to-Current-Efficiencies Measurement

The photoanode incident-photon-to-current-efficiencies (IPCEs) measure at 1.23 V vs RHE to further confirm that the photocurrent was improved after the amorphous CoO_x layer coated. Compared with the bare hematite, the hematite decorated with amorphous CoO_x showed that IPCE value was enhanced substantially.

At 400 nm, Fe_2O_3 showed IPCE of ca. 22% and drops to zero at wavelengths longer than 560 nm, which is consistent with the energetics of the hematite band gap. However, 2-CoO_x/Fe_2O_3 has a much higher IPCE, of ca. 50%. This value is even higher than the IPCE of photo-assisted electrodeposition of Co-Pi/Fe_2O_3 which was ca.40%.[113] The IPCE of 2-CoO_x/Fe_2O_3 still showed a weak value for the wavelengths above 600 nm, even though absorption occurs (Figure 42) because absorption is most likely due to defects.

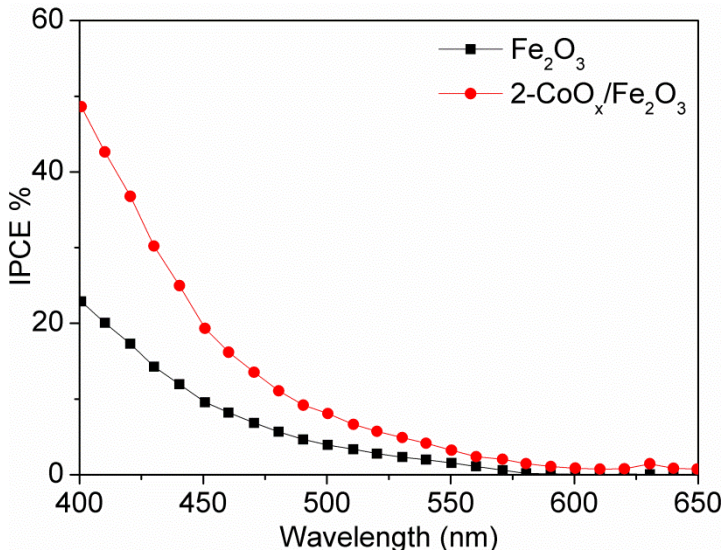

Figure 48: IPCE performance of Fe_2O_3 and 2-CoO_x/Fe_2O_3 at 1.23V vs RHE.

4.4: Conclusions

In summary, we used a UV light deposition method to load amorphous CoO_x on the surface of Fe_2O_3 nanorod arrays, achieving a higher photocurrent compared with untreated Fe_2O_3. After loaded with CoO_x, the photocurrent density increased from 0.6 for Fe_2O_3 nanorods to 1.5 mA/cm^2 at 1.23 V versus RHE. The structure and chemical state of amorphous CoO_x layer was studied and EIS measurements were used to get insight of the mechanism of photocurrent enhanced. First, the amorphous CoO_x layer improves the photo response, due to defects increased on the surface, however IPCE shows that this extra absorption does not give more photocurrent. Second, it could enhance the carrier transfer in the bulk and interface between Fe_2O_3 and CoO_x, which is supported by EIS measurements. Third, CoO_x could act as a good catalyst for water oxidation on the surface of Fe_2O_3, however recent work suggests that the main role of Co is to reduce recombination. In summary, this work illustrates a new method to load amorphous oxide on the surface of Fe_2O_3 which show improved photoelectrochemical efficiency, and offer a new guide to design novel highly efficient photoanodes.

Chapter 5

Summary and future direction

5.1: Summary

Although Fe_2O_3 is a promising material to achieve high efficiency PEC water splitting, pristine Fe_2O_3 suffers from low efficiency due to rapid recombination and slow redox catalysis. The aim of this project was to develop several methods to improve the photon-to-electron and photon-to-oxygen conversion efficiency of Fe_2O_3 by doping a homojunction, heterojunction and addition of a co-catalyst.

Specifically, two different morphologies of a Fe_2O_3 photoanode, nanoparticle and nanorod, were synthesized using hydrothermal methods. Analogues were synthesized incorporating Sn and Co as dopants to construct new homojunctions with double layered structure. The Co/Sn/Fe_2O_3 photoanode showed the highest photocurrent with ca. 2.5 times enhancement relative to bare Fe_2O_3. The Co/Sn/Fe_2O_3 n-n homojunction could increase the density of carriers, and improve the charge separation and reduce resistance in the charge transfer across the electrode and electrolyte.

Inspired by the homojunction structure, a three component heterojunction, Cu_2O/CdS/Fe_2O_3 was prepared. The self-oxidation of CdS could be inhibited by the heterojunction structure and CdS could act as hole mediator to support stepwise charge transfer between Cu_2O and Fe_2O_3.

For both photocatalytic and PEC water splitting, the redox reactions always take place on the surface of the electrode and clearly a more active surface is beneficial for catalysis reaction. Co oxide has been proven to decrease the overpotential of O_2 evolution on the surface of Fe_2O_3. Typically, Co oxide is loaded by electrodeposition or impregnation method, whereas, we have used a UV light deposition method to load amorphous Co oxide on the surface of Fe_2O_3 nanorod arrays, achieving a higher photocurrent compared with untreated Fe_2O_3.

5.2: Future direction

Fe_2O_3 is cheap, non-toxic and stable and has promise to achieve solar-to-chemical energy conversion and help solve the energy and environmental crisis. However, some defects of Fe_2O_3 still limit the efficiency and if we could solve these problems, the industrialization of Fe_2O_3 photoelectrodes will be achievable in the future.

To be specific, (1) the surface of Fe_2O_3 is not ideal for oxygen evolution as it has a high overpotential. Co-catalyst modification is a good direction to increase O_2 release. Some oxidants, like CoO_X, RuO_X, IrO_X NiO_X, and some phosphates such as Co-Pi and some noble metals have been proved to be beneficial for overpotential decrease. (2) As the hole transfer speed and distance in Fe_2O_3 is slow and short, lots of holes will be recombined with electrons rather than move to surface. Doping with metal or non-metal elements could increase the conductivity of Fe_2O_3. (3) Charge transfer from Fe_2O_3 to the TCO supporting electrode was limited due to contact area and to increase the contact area and decrease the transmission distance from Fe_2O_3 to TCO would improve the separation efficiency of photo-generated carriers. (4) The mechanism of PEC water splitting of Fe_2O_3 is still not clear, and to find out the key step of this reaction is also an important work to enhance the activity. DFT and transient absorption spectroscopy could give us some guidelines to improve the PEC reaction.

Although PEC water splitting is still some way from commercialization, the technology is progressing. We will see one day in the future that PEC could make a significant contribution to the energy needs of society.

Chapter 6

Experimental

6.1: Materials and Reagents

Iron (III) chloride ($FeCl_3$ 98%), Tin (IV) chloride pentahydrate ($SnCl_4 \cdot 5H_2O$ 98%), Cobalt (II) chloride hexahydrate ($CoCl_2 \cdot 6H_2O$ 98%), Cobalt 2-ethylhexanoate (65 wt.% in mineral spirits), copper(II) acetate monohydrate ($Cu(CO_2CH_3)_2 \cdot H_2O$ 98%), Sodium sulfide nonahydrate ($NaS \cdot 9H_2O$ 98%), and Cadmium acetate dehydrate ($Cd(CO_2CH_3)_2 \cdot 2H_2O$ 98%) were purchased from Aldrich. Sodium hydroxide (NaOH 98%) was purchased from Fisher. Millipore water was obtained from chemistry department of UoY. All of the chemicals were used without further purification.

Sheets of fluorine doped tin oxide coated glass were purchased from Sigma Aldrich (7 Ω/sq, 30 x 30 cm), and cut into 1 x 3 cm slides. Before use, slides were cleaned by sonication in acetone, methanol, and deionized water for half an hour, separately, and dried in a nitrogen stream.

6.2: Techniques

6.2.1: Powder X-ray Diffraction (PXRD)

Powder X-ray Diffraction (PXRD) of all samples were measured by Bruker-AXS D8 Advance instrument fitted with a Lynxeye detector using Cu Kα radiation (λ=1.5406 Å). The accelerating voltage and the applied current were 40 kV and 40 mA, respectively. Data was collected from 10 – 90° 2θ, with 0.02° step size and a scan speed of 0.1 seconds per step.

6.2.2: Scanning Electron Microscopy

SEM images were obtained using a JEOL 2000FEI scanning electron microscope. Prior to imaging, samples were put on an adhesive carbon tab which was supported on an aluminium stub.

6.2.3: Transmission Electron Microscopy

TEM and HRTEM images were obtained by a Tecnai F30 instrument at an accelerating voltage of 500 kV. FTO film samples were scraped off the slide, then ground in methanol and sonicated for 15 minutes to disperse. One drop of the dispersion was deposited onto 3 mm holey carbon coated copper grids and allowed to dry in air.

6.2.4: X-ray Photoelectron Spectroscopy

XPS spectra were carried out on a VG ESCALAB 250 XPS System with a monochromatized Al Ka X–ray sources (15 kv 200 W 500 um pass energy = 20 eV). All binding energies were referenced to the C1s peak at 284.6 eV of surface adventitious carbon.

6.2.5: UV-vis Transmission Spectroscopy

UV-Visible transmission spectra was recorded on an Ocean Optics HR2000+ High Resolution Spectrometer with DH-2000-BAL Deuterium/Helium light source (200 – 1100 nm). Spectra were recorded using Spectra Suite software from an average of 10 scans, an integration time of 20 seconds and box car smoothing width of 20 nm.

6.2.6: Photoelectrochemical measurements

Electrochemical measurements were carried out in 1.0 M NaOH aqueous solution. using a three-electrode photoelectrochemical cell (PEC) adapted with a quartz window, a Pt counter electrode, and Ag/AgCl/NaCl (3.0 M) reference electrode. The area at the top of the photoanode was scraped to exposure the FTO film and covered with a copper sheet. The photoanode was put in the cell as a working electrode to observe its PEC water oxidation response which was recorded by a BAS Epsilon workstation. The photocurrent-potential curve was measured under solar light

generated by a Cairn 150 W xenon lamp coupled with AM1.5G filter. Light intensity of the simulated light was adjusted to 1 sun (100mW/cm^2).

6.2.7: Impedance Spectroscopy

The impedance spectroscopy measurements were performed on a Zhnner potentiostat, Bio-logical 300 potentiostat and Bio-logical 150 potentiostat. The Mott-Schottky plots were measured in the dark at 100 Hz frequency. The Nyquist plots were measured at 1.23 V vs RHE with the frequency range being modulated between 100 kHz to 0.1 Hz at amplitude frequency 10 mV under 1-sun light generated by a 150W xenon lamp coupled with an AM 1.5G filter.

6.2.7: Incident Photon to Current conversion Efficiency (IPCE) Experiments

The incident photon to current conversion efficiency (IPCE) experiments with the hematite samples were performed in 1 M NaOH electrolyte at 1.23 V vs RHE using a light (Cairn 150 W xenon lamp) coupled to a monochromator (Cairn) with a slit width of 2 nm.

6.3: Synthetic methods

6.3.1: Fabrication of Fe_2O_3 nanoparticles photoanode

A FTO glass (1 cm × 3 cm) was cleaned by sonication in acetone, methanol, and deionized water for half an hour, separately, and dried in a nitrogen stream. The clean FTO was then placed in an 20 mL hydrothermal reactor, with a 15 mL aqueous solution containing $FeCl_3$ (0.25 mmol). The autoclave was placed at 180 °C for 1.2 h using a ramp rate of 5 °C/min. After cooling to room temperature in furnace, the

product was collected and rinsed with deionized water and dried in a nitrogen atmosphere stream, and annealed in air at 550 °C for 2 h and 800 °C for 20 min.

6.3.2: Fabrication of Sn doped Fe_2O_3 and Co doped Fe_2O_3nanoparticles photoanode

The synthesis of Sn/Fe_2O_3 and Co/Fe_2O_3 was similar to Fe_2O_3 except that $SnCl_4$•$5H_2O$ (0.005 mmol) and $CoCl_2$•$6H_2O$ (0.002mmol) was added into the autoclave as dopant for hydrothermal reaction.

6.3.3: Fabrication of Fe_2O_3 homojunction photoanode

The synthesis of Co/Sn/Fe_2O_3 was achieved using a two-step hydrothermal reaction. First, the clean FTO (1 cm × 3 cm) was placed in a 20 mL hydrothermal reactor, with a 15 mL aqueous solution containing $FeCl_3$ (0.25 mmol) and $SnCl_4$•$5H_2O$ (0.005 mmol). The autoclave was placed at 180 °C for 1.2 h using a ramp rate of 5 °C/min. After cooling to room temperature in furnace, the product was collected and rinsed with deionized water and dried in a nitrogen atmosphere stream, and annealed in air at 550 °C for 2 h. Then, the FTO coated with Sn/Fe_2O_3 was placed in an autoclave, with a 20 mL aqueous solution containing $FeCl_3$ (0.25 mmol) and $CoCl_2$•$6H_2O$ (0.002 mmol). The autoclave was placed at 180 °C for 1.2 h using a ramp rate of 5 °C/min. After cooling to room temperature in furnace, the product was collected and rinsed with deionized water and dried in a nitrogen atmosphere stream, and annealed in air at 550 °C for 2 h and 800 °C for 20 min to obtain Co/Sn/Fe_2O_3 photoanode.

The way to synthesize Sn/Co/is identical but the order of Sn and Co processes is reversed.

6.3.4: Fabrication of Fe_2O_3 nanorods array photoanode

A FTO glass (1 cm × 3 cm) was cleaned by sonication in acetone, methanol, and deionized water for half an hour, separately, and dried in a nitrogen stream. The clean FTO was then placed in a 20 mL hydrothermal reactor, with a 15 mL aqueous solution containing $FeCl_3$ (0.15 M). The autoclave was placed at 100 °C for 6 h using a ramp rate of 5 °C/min. After cooling to room temperature in furnace, the product was collected and rinsed with deionized water and dried in a nitrogen atmosphere stream, and annealed in air at 550 °C for 2 h and 800 °C for 20 min.

6.3.5: Fabrication of CdS/Fe_2O_3 and Cu_2O/Fe_2O_3 nanorod array heterojunction photoanode

Fe_2O_3 nanorods array electrode was dipped in a solution of 7 mL $Cd(Ac)_2$ in ethanol (25 mM) for 1 min, and then dried with N_2 stream. The electrode was then stand in 7 mL aqueous Na_2S solution (25 mM) for 1 min, rinsed with distilled water and dried with N_2. This cycle was repeated 5 times. The electrode was finally heated under argon at 400 ^oC for 0.5h with a ramp rate of 1 ^oC min^{-1} to obtain the CdS/Fe_2O_3 electrode.

Fe_2O_3 nanorods array electrode was stood in 7ml 50mM $Cu(Ac)_2$ solution for 40s. Then, the electrode was stood in 7 mL aqueous 1M NaOH solution and heated in 60^oC for 1 h. After that, the electrode was sonicated in millipore water for 1h. The electrode was finally heated under argon at 500 ^oC for 2h with a ramp rate of 10 ^oC min^{-1} to obtain Cu_2O/Fe_2O_3.

6.3.5: Fabrication of $CdS/Cu_2O/Fe_2O_3Fe_2O_3$ nanorods array heterojunction photoanode

Fe_2O_3 nanorods array electrode was dipped in a solution of 7 mL $Cd(Ac)_2$ in ethanol (25 mM) for 1 min, and then dried with N_2 stream. The electrode was then stood in 7

mL aqueous Na_2S solution (25 mM) for 1 min, rinsed with distilled water and dried with N_2. This cycle was repeated 5 times. The electrode was finally heated under argon at 400 ^oC for 0.5h with a ramp rate of 1 $^oC\ min^{-1}$ to obtain the CdS/Fe_2O_3 electrode. The obtained CdS/Fe_2O_3 was stood in 7ml 50mM $Cu(Ac)_2$ solution for 40s. Then, the electrode was stood in 7 mL aqueous 1M NaOH solution and heated in 60 ^oC for 1 h. After that, the electrode was sonicated in millipore water for 1h. The electrode was finally heated under argon at 500 ^oC for 2h with a ramp rate of 10 $^oC\ min^{-1}$ to obtain $Cu_2O/CdS/Fe_2O_3$.

6.3.6: Decoration of CoO_x on Fe_2O_3 nanorods array photoanode

Cobalt 2-ethylhexanoate was diluted to 0.5 mM in hexane. Fe_2O_3 nanorods array electrode were dipped into the 0.5 mM cobalt 2-ethylhexanoate hexane solution for 0.5 min, 1 min, 2 min, 5 min and 10 min, and then irradiated with UV light (17 W) for 6 h, heated in 373K for 1 h.

Abbreviations

2-CoO_X/Fe_2O_3 ─ Iron oxide was placed in Co-2-ethylhexanoate for two minutes.

AM 1.5G ─ Air Mass 1.5 Global spectrum

Ac ─ Acetate

APCVD ─ Atmospheric Pressure Chemical Vapor Deposition

CB ─ Conduction Band

Co/Fe_2O_3 ─ Cobalt doped iron oxide

$Co/Sn/Fe_2O_3$ ─ homojunction composited with cobalt doped iron oxide and tin doped iron oxide and cobalt doped iron oxide on the upper layer.

CPE ─ Constant Phase Elements

EC ─ Equivalent Circle

EIS ─ Electrochemical Impedance Spectroscopy

FB ─ Flat Band potential

FTO ─ Fluorine Doped Tin Oxide

HRTEM ─ High Revolution Transmission Electron Microscopy

IPCE ─ Incident Photon to Current Conversion Efficiency

J–V ─ Current–Voltage

LSV ─ Linear Sweep Voltammetry

M-S ─ Mott-Schottky plot

ND ─ Donor Density

OER ─ Oxygen Evolution Reaction

PEC ─ Photoelectrochemistry

PV─ Photovoltage

R ─ Resistances

RHE ─ Reversible Hydrogen Electrode

SEM ─ Scanning Electron Microscopy

Sn/Fe_2O_3 ─ Tin doped iron oxide

$Sn/Co/Fe_2O_3$ ─ homojunction composited with cobalt doped iron oxide and tin doped iron oxide and tin doped iron oxide on the upper layer

TEM ─ Transmission Electron MicroscopyUV ─ Ultraviolet Light

UV-vis ─ Ultraviolet and Visible light

VB ─ Valence Band

WOC ─ Waste Organic Carbon

XPS ─ X-ray Photoelectron Spectroscopy

XRD ─ X-ray Diffraction

References

1. Panwar NL, Kaushik SC, Kothari S. Role of renewable energy sources in environmental protection: A review. *Renew. Sustainable Energy Rev.* 2011, **15**(3)**:** 1513-1524.

2. Armaroli N, Balzani V. The future of energy supply: Challenges and opportunities. *Angew. Chem. Int. Ed.* 2007, **46**(1-2)**:** 52-66.

3. Dincer I. Renewable energy and sustainable development: a crucial review. *Renew. Sustainable Energy Rev.* 2000, **4**(2)**:** 157-175.

4. Lewis NS, Nocera DG. Powering the planet: chemical challenges in solar energy utilization. *Proc. Natl. Acad. Sci. U. S. A.* 2006, **103**(43)**:** 15729-15735.

5. Izumi Y. Recent advances in the photocatalytic conversion of carbon dioxide to fuels with water and/or hydrogen using solar energy and beyond. *Coord. Chem. Rev.* 2013, **257**(1)**:** 171-186.

6. Varghese OK, Paulose M, Latempa TJ, Grimes CA. High-rate solar photocatalytic conversion of CO2 and water vapor to hydrocarbon fuels. *Nano lett.* 2009, **9**(2)**:** 731-737.

7. Kumar B, Llorente M, Froehlich J, Dang T, Sathrum A, Kubiak CP. Photochemical and photoelectrochemical reduction of CO2. *Annu. Rev. Phys. Chem.* 2012, **63:** 541-569.

8. Tu W, Zhou Y, Zou Z. Photocatalytic conversion of CO(2) into renewable hydrocarbon fuels: state-of-the-art accomplishment, challenges, and prospects. *Adv. Mater.* 2014, **26**(27)**:** 4607-4626.

9. Morris AJ, Meyer GJ, Fujita E. Molecular approaches to the photocatalytic reduction of carbon dioxide for solar fuels. *Acc. Chem. Res.* 2009, **42**(12)**:** 1983-1994.

10. Zhang T, Lin W. Metal-organic frameworks for artificial photosynthesis and photocatalysis. *Chem. Soc. Rev.* 2014, **43**(16)**:** 5982-5993.

11. Hisatomi T, Kubota J, Domen K. Recent advances in semiconductors for photocatalytic and photoelectrochemical water splitting. *Chem. Soc. Rev.* 2014, **43**(22)**:** 7520-7535.

12. Fujishima A, Honda K. Electrochemical Photolysis of Water at a Semiconductor Electrode. *Nature* 1972, **238**(5358)**:** 37-38.

13. Fontecave M. Energy for a Sustainable World. From the Oil Age to a Sun-Powered Future. By Nicola Armaroli and Vincenzo Balzani. *Angew. Chem. Int. Ed.* 2011, **50**(30)**:** 6704-6705.

14. Abhat A. Low temperature latent heat thermal energy storage: Heat storage materials. *Solar Energy* 1983, **30**(4)**:** 313-332.

15. Kronik L, Shapira Y. Surface photovoltage phenomena: theory, experiment, and applications. *Surf. Sci. Rep.* 1999, **37**(1-5)**:** 1-206.

16. Hagfeldt A, Boschloo G, Sun LC, Kloo L, Pettersson H. Dye-Sensitized Solar Cells. *Chem. Rev.* 2010, **110**(11)**:** 6595-6663.

17. Gratzel M. Photoelectrochemical cells. *Nature* 2001, **414**(6861)**:** 338-344.

18. Tong H, Ouyang SX, Bi YP, Umezawa N, Oshikiri M, Ye JH. Nano-photocatalytic Materials: Possibilities and Challenges. *Adv. Mater.* 2012, **24**(2)**:** 229-251.

19. Huang HW, Lin JJ, Zhu GB, Weng YX, Wang XX, Fu XZ*, et al.* A Long-Lived Mononuclear Cyclopentadienyl Ruthenium Complex Grafted onto Anatase TiO2 for Efficient CO2 Photoreduction. *Angew. Chem. Int. Ed.* 2016, **55**(29)**:** 8314-8318.

20. Youngblood WJ, Lee SHA, Maeda K, Mallouk TE. Visible Light Water Splitting Using Dye-Sensitized Oxide Semiconductors. *Acc. Chem. Res.* 2009, **42**(12)**:** 1966-1973.

21. Roy SC, Varghese OK, Paulose M, Grimes CA. Toward Solar Fuels: Photocatalytic Conversion of Carbon Dioxide to Hydrocarbons. *ACS nano* 2010, **4**(3)**:** 1259-1278.

22. Habisreutinger SN, Schmidt-Mende L, Stolarczyk JK. Photocatalytic Reduction of CO2 on TiO2 and Other Semiconductors. *Angew. Chem. Int. Ed.* 2013, **52**(29)**:** 7372-7408.

23. Palmisano G, Augugliaro V, Pagliaro M, Palmisano L. Photocatalysis: a promising route for 21st century organic chemistry. *Chem. Commun.* 2007(33)**:** 3425-3437.

24. Linsebigler AL, Lu GQ, Yates JT. PHOTOCATALYSIS ON TIO2 SURFACES - PRINCIPLES, MECHANISMS, AND SELECTED RESULTS. *Chem. Rev.* 1995, **95**(3)**:** 735-758.

25. Fox MA, Dulay MT. HETEROGENEOUS PHOTOCATALYSIS. *Chem. Rev.* 1993, **93**(1)**:** 341-357.

26. Lin YJ, Yuan GB, Sheehan S, Zhou S, Wang DW. Hematite-based solar water splitting: challenges and opportunities. *Energy Environ. Sci.* 2011, **4**(12)**:** 4862-4869.

27. Wang HL, Zhang LS, Chen ZG, Hu JQ, Li SJ, Wang ZH*, et al.* Semiconductor heterojunction photocatalysts: design, construction, and photocatalytic performances. *Chem. Soc. Rev.* 2014, **43**(15)**:** 5234-5244.

28. Zhou W, Fu HG. Mesoporous TiO2: Preparation, Doping, and as a Composite for Photocatalysis. *ChemCatChem* 2013, **5**(4)**:** 885-894.

29. Yang J, Wang D, Han H, Li C. Roles of cocatalysts in photocatalysis and photoelectrocatalysis. *Acc. Chem. Res.* 2013, **46**(8)**:** 1900-1909.

30. Kudo A, Miseki Y. Heterogeneous photocatalyst materials for water splitting. *Chem. Soc. Rev.* 2009, **38**(1)**:** 253-278.

31. Kang D, Kim TW, Kubota SR, Cardiel AC, Cha HG, Choi KS. Electrochemical Synthesis of Photoelectrodes and Catalysts for Use in Solar Water Splitting. *Chem. Rev.* 2015, **115**(23)**:** 12839-12887.

32. Iwase A, Ng YH, Ishiguro Y, Kudo A, Amal R. Reduced Graphene Oxide as a Solid-State Electron Mediator in Z-Scheme Photocatalytic Water Splitting under Visible Light. *J. Am. Chem. Soc.* 2011, **133**(29)**:** 11054-11057.

33. Kato H, Hori M, Konta R, Shimodaira Y, Kudo A. Construction of Z-scheme type heterogeneous photocatalysis systems for water splitting into H-2 and O-2 under visible light irradiation. *Chem. Lett.* 2004, **33**(10)**:** 1348-1349.

34. Zhang Z, Yates JT. Band Bending in Semiconductors: Chemical and Physical Consequences at Surfaces and Interfaces. *Chem. Rev.* 2012, **112**(10)**:** 5520-5551.

35. Santato C, Ulmann M, Augustynski J. Photoelectrochemical properties of nanostructured tungsten trioxide films. *J. Phys. Chem. B* 2001, **105**(5)**:** 936-940.

36. Liu X, Wang FY, Wang Q. Nanostructure-based WO3 photoanodes for photoelectrochemical water splitting. *Phys. Chem. Chem. Phys.* 2012, **14**(22)**:** 7894-7911.

37. Huang JW, Ding Y, Luo X, Feng YY. Solvation effect promoted formation of p-n junction between WO3 and FeOOH: A high performance photoanode for water oxidation. *J. Catal.* 2016, **333:** 200-206.

38. Kudo A, Ueda K, Kato H, Mikami I. Photocatalytic O-2 evolution under visible light irradiation on BiVO4 in aqueous AgNO3 solution. *Catal. Lett.* 1998, **53**(3-4)**:** 229-230.

39. Liang YQ, Tsubota T, Mooij LPA, van de Krol R. Highly Improved Quantum Efficiencies

for Thin Film BiVO4 Photoanodes. *J. Phys. Chem. C* 2011, **115**(35)**:** 17594-17598.

40. Hong SJ, Lee S, Jang JS, Lee JS. Heterojunction BiVO4/WO3 electrodes for enhanced photoactivity of water oxidation. *Energy Environ. Sci.* 2011, **4**(5)**:** 1781.

41. Zhong DK, Choi S, Gamelin DR. Near-Complete Suppression of Surface Recombination in Solar Photoelectrolysis by "Co-Pi" Catalyst-Modified W:BiVO4. *J. Am. Chem. Soc.* 2011, **133**(45)**:** 18370-18377.

42. Pilli SK, Furtak TE, Brown LD, Deutsch TG, Turner JA, Herring AM. Cobalt-phosphate (Co-Pi) catalyst modified Mo-doped BiVO4 photoelectrodes for solar water oxidation. *Energy Environ. Sci.* 2011, **4**(12)**:** 5028-5034.

43. Kennedy JH, Frese KW. PHOTOOXIDATION OF WATER AT ALPHA-FE2O3 ELECTRODES. *J. Electrochem. Soc.* 1977, **124**(3)**:** C130-C130.

44. Bassi PS, Gurudayal, Wong LH, Barber J. Iron based photoanodes for solar fuel production. *Phys. Chem. Chem. Phys..* 2014, **16**(24)**:** 11834-11842.

45. Sivula K, Le Formal F, Gratzel M. Solar Water Splitting: Progress Using Hematite (alpha-Fe2O3) Photoelectrodes. *ChemSusChem* 2011, **4**(4)**:** 432-449.

46. Shinde PS, Choi SH, Kim Y, Ryu J, Jang JS. Onset potential behavior in alpha-Fe2O3 photoanodes: the influence of surface and diffusion Sn doping on the surface states. *Phys. Chem. Chem. Phys.* 2016, **18**(4)**:** 2495-2509.

47. Tilley SD, Cornuz M, Sivula K, Gratzel M. Light-Induced Water Splitting with Hematite: Improved Nanostructure and Iridium Oxide Catalysis. *Angew. Chem. Int. Ed.* 2010, **49**(36)**:** 6405-6408.

48. Sivula K, Le Formal F, Gratzel M. Solar water splitting: progress using hematite (alpha-Fe(2) O(3)) photoelectrodes. *ChemSusChem* 2011, **4**(4)**:** 432-449.

49. Li ZS, Luo WJ, Zhang ML, Feng JY, Zou ZG. Photoelectrochemical cells for solar hydrogen production: current state of promising photoelectrodes, methods to improve their properties, and outlook. *Energy Environ. Sci.* 2013, **6**(2)**:** 347-370.

50. Cao D, Luo W, Li M, Feng J, Li Z, Zou Z. A transparent Ti4+ doped hematite photoanode protectively grown by a facile hydrothermal method. *CrystEngComm* 2013, **15**(13)**:** 2386.

51. Ling Y, Li Y. Review of Sn-Doped Hematite Nanostructures for Photoelectrochemical Water Splitting. *Part. Part. Syst. Char.* 2014, **31**(11)**:** 1113-1121.

52. Cesar I, Kay A, Martinez JAG, Gratzel M. Translucent thin film Fe2O3 photoanodes for efficient water splitting by sunlight: Nanostructure-directing effect of Si-doping. *J. Am. Chem. Soc.* 2006, **128**(14)**:** 4582-4583.

53. Deng JJ, Zhong J, Pu AW, Zhang D, Li M, Sun XH*, et al.* Ti-doped hematite nanostructures for solar water splitting with high efficiency. *J. Appl. Phys.* 2012, **112**(8).

54. Liu Y, Yu YX, Zhang WD. Photoelectrochemical properties of Ni-doped Fe2O3 thin films prepared by electrodeposition. *Electrochim. Acta* 2012, **59:** 121-127.

55. Meng XY, Qin GW, Li S, Wen XH, Ren YP, Pei WL*, et al.* Enhanced photoelectrochemical activity for Cu and Ti doped hematite: The first principles calculations. *Appl. Phys. Lett.* 2011, **98**(11).

56. Lin Y, Xu Y, Mayer MT, Simpson ZI, McMahon G, Zhou S*, et al.* Growth of p-type hematite by atomic layer deposition and its utilization for improved solar water splitting. *J. Am. Chem. Soc.* 2012, **134**(12)**:** 5508-5511.

57. Mirbagheri N, Wang DG, Peng C, Wang JQ, Huang Q, Fan CH*, et al.* Visible Light Driven Photoelectrochemical Water Oxidation by Zn- and Ti-Doped Hematite Nanostructures. *ACS Catal.* 2014, **4**(6)**:** 2006-2015.

58. Kay A, Cesar I, Gratzel M. New benchmark for water photooxidation by nanostructured alpha-Fe2O3 films. *J. Am. Chem. Soc.* 2006, **128**(49)**:** 15714-15721.

59. Li L, Yu Y, Meng F, Tan Y, Hamers RJ, Jin S. Facile solution synthesis of alpha-FeF3.3H2O nanowires and their conversion to alpha-Fe2O3 nanowires for photoelectrochemical application. *Nano lett.* 2012, **12**(2)**:** 724-731.

60. Kim JY, Magesh G, Youn DH, Jang JW, Kubota J, Domen K*, et al.* Single-crystalline, wormlike hematite photoanodes for efficient solar water splitting. *Sci. Rep.*2013, **3:** 2681.

61. Zhong DK, Sun J, Inumaru H, Gamelin DR. Solar water oxidation by composite catalyst/alpha-Fe(2)O(3) photoanodes. *J. Am. Chem. Soc.* 2009, **131**(17)**:** 6086-6087.

62. Wang Z, Liu G, Ding C, Chen Z, Zhang F, Shi J*, et al.* Synergetic Effect of Conjugated Ni(OH)2/IrO2Cocatalyst on Titanium-Doped Hematite Photoanode for Solar Water Splitting. *J. Phys. Chem. C* 2015, **119**(34)**:** 19607-19612.

63. Ahmed MG, Kandiel TA, Ahmed AY, Kretschmer I, Rashwan F, Bahnemann D. Enhanced Photoelectrochemical Water Oxidation on Nanostructured Hematite Photoanodes via p-CaFe2O4/n-Fe2O3Heterojunction Formation. *J. Phys. Chem. C*

2015, **119**(11)**:** 5864-5871.

64. Kang J, Kuang Q, Xie ZX, Zheng LS. Fabrication of the SnO2/alpha-Fe2O3 Hierarchical Heterostructure and Its Enhanced Photocatalytic Property. *J. Phys. Chem. C* 2011, **115**(16)**:** 7874-7879.

65. Le Formal F, Tetreault N, Cornuz M, Moehl T, Gratzel M, Sivula K. Passivating surface states on water splitting hematite photoanodes with alumina overlayers. *Chem. Sci.* 2011, **2**(4)**:** 737-743.

66. Xi LF, Bassi PS, Chiam SY, Mak WF, Tran PD, Barber J*, et al.* Surface treatment of hematite photoanodes with zinc acetate for water oxidation. *Nanoscale* 2012, **4**(15)**:** 4430-4433.

67. Li JT, Meng FK, Suri S, Ding WQ, Huang FQ, Wu NQ. Photoelectrochemical performance enhanced by a nickel oxide-hematite p-n junction photoanode. *Chem. Commun.* 2012, **48**(66)**:** 8213-8215.

68. Hou Y, Zuo F, Dagg A, Feng P. A three-dimensional branched cobalt-doped alpha-Fe2O3 nanorod/MgFe2O4 heterojunction array as a flexible photoanode for efficient photoelectrochemical water oxidation. *Angew. Chem. Int. Ed.* 2013, **52**(4)**:** 1248-1252.

69. McDonald KJ, Choi K-S. Synthesis and Photoelectrochemical Properties of Fe2O3/ZnFe2O4Composite Photoanodes for Use in Solar Water Oxidation. *Chem. Mater.* 2011, **23**(21)**:** 4863-4869.

70. Wang H, Zhang L, Chen Z, Hu J, Li S, Wang Z*, et al.* Semiconductor heterojunction photocatalysts: design, construction, and photocatalytic performances. *Chem. Soc. Rev.* 2014, **43**(15)**:** 5234-5244.

71. Dare-Edwards MP, Goodenough JB, Hamnett A, Trevellick PR. Electrochemistry and photoelectrochemistry of iron(III) oxide. *J. Chem. Soc., Faraday Trans. 1* 1983, **79**(9)**:** 2027.

72. Hou Y, Zuo F, Dagg A, Feng P. A Three-Dimensional Branched Cobalt-Doped α-Fe2O3Nanorod/MgFe2O4Heterojunction Array as a Flexible Photoanode for Efficient Photoelectrochemical Water Oxidation. *Angew. Chem. Int. Ed.* 2013, **125**(4)**:** 1286-1290.

73. Ling Y, Wang G, Wheeler DA, Zhang JZ, Li Y. Sn-doped hematite nanostructures for photoelectrochemical water splitting. *Nano letters* 2011, **11**(5)**:** 2119-2125.

74. Liu Y, Yu Y-X, Zhang W-D. Photoelectrochemical properties of Ni-doped Fe2O3 thin

films prepared by electrodeposition. *Electrochim. Acta* 2012, **59:** 121-127.

75. Gu Q, Long J, Zhou Y, Yuan R, Lin H, Wang X. Single-site tin-grafted anatase TiO2 for photocatalytic hydrogen production: Toward understanding the nature of interfacial molecular junctions formed in semiconducting composite photocatalysts. *J. Catal.* 2012, **289:** 88-99.

76. Vayssieres L, Beermann N, Lindquist S-E, Hagfeldt A. Controlled Aqueous Chemical Growth of Oriented Three-Dimensional Crystalline Nanorod Arrays: Application to Iron(III) Oxides. *Chem. Mater.* 2001, **13**(2)**:** 233-235.

77. Saremi-Yarahmadi S, Wijayantha KGU, Tahir AA, Vaidhyanathan B. Nanostructured α-Fe2O3Electrodes for Solar Driven Water Splitting: Effect of Doping Agents on Preparation and Performance. *J. Phys. Chem. C* 2009, **113**(12)**:** 4768-4778.

78. Miller EL, Paluselli D, Marsen B, Rocheleau RE. Low-temperature reactively sputtered iron oxide for thin film devices. *Thin Solid Films* 2004, **466**(1-2)**:** 307-313.

79. Pal B, Sharon M. Photocatalytic degradation of salicylic acid by colloidal Fe2O3 particles. *J. Chem. Technol. Biotechnol.* 1998, **73**(3)**:** 269-273.

80. Sadigh B, Erhart P, Aberg D, Trave A, Schwegler E, Bude J. First-principles calculations of the Urbach tail in the optical absorption spectra of silica glass. *Phys. Rev. Lett.* 2011, **106**(2)**:** 027401.

81. Redfield D. Effect of Defect Fields on the Optical Absorption Edge. *Phys. Rev.* 1963, **130**(3)**:** 916-918.

82. Pan Y, Inam F, Zhang M, Drabold DA. Atomistic origin of urbach tails in amorphous silicon. *Phys. Rev. Lett.* 2008, **100**(20)**:** 206403.

83. Huang H, Lin J, Fan L, Wang X, Fu X, Long J. Heteroatomic Ni, Sn Clusters-Grafted Anatase TiO2Photocatalysts: Structure, Electron Delocalization, and Synergy for Solar Hydrogen Production. *J. Phys. Chem. C* 2015, **119**(19)**:** 10478-10492.

84. Li J, Meng F, Suri S, Ding W, Huang F, Wu N. Photoelectrochemical performance enhanced by a nickel oxide-hematite p-n junction photoanode. *Chem. Commun.* 2012, **48**(66)**:** 8213-8215.

85. Qin D-D, Tao C-L, In S-i, Yang Z-Y, Mallouk TE, Bao N*, et al.* Facile Solvothermal Method for Fabricating Arrays of Vertically Oriented α-Fe2O3Nanowires and Their Application in Photoelectrochemical Water Oxidation. *Energy Fuels* 2011, **25**(11)**:** 5257-5263.

86. Gonçalves RH, Leite ER. The colloidal nanocrystal deposition process: an advanced method to prepare high performance hematite photoanodes for water splitting. *Energy Environ. Sci.* 2014, **7**(7)**:** 2250.

87. Yang T, Sang L, Ding F, Zhang J, Liu X. Three- and four-electrode EIS analysis of water stable lithium electrode with solid electrolyte plate. *Electrochim. Acta* 2012, **81:** 179-185.

88. Mulmudi HK, Mathews N, Dou XC, Xi LF, Pramana SS, Lam YM*, et al.* Controlled growth of hematite (α-Fe2O3) nanorod array on fluorine doped tin oxide: Synthesis and photoelectrochemical properties. *Electrochem. Commun.* 2011, **13**(9)**:** 951-954.

89. Xi L, Tran PD, Chiam SY, Bassi PS, Mak WF, Mulmudi HK*, et al.* Co3O4-Decorated Hematite Nanorods As an Effective Photoanode for Solar Water Oxidation. *J. Phys. Chem. C* 2012, **116**(26)**:** 13884-13889.

90. Trindade T, O'Brien P, Pickett NL. Nanocrystalline Semiconductors: Synthesis, Properties, and Perspectives. *Chem. Mater.* 2001, **13**(11)**:** 3843-3858.

91. Jing D, Guo L. A novel method for the preparation of a highly stable and active CdS photocatalyst with a special surface nanostructure. *J. Phys. Chem. B* 2006, **110**(23)**:** 11139-11145.

92. Fermin DJ, Ponomarev EA, Peter LM. A kinetic study of CdS photocorrosion by intensity modulated photocurrent and photoelectrochemical impedance spectroscopy. *J. Electroanal. Chem.* 1999, **473**(1-2)**:** 192-203.

93. Shi Y, Li H, Wang L, Shen W, Chen H. Novel alpha-Fe2O3/CdS cornlike nanorods with enhanced photocatalytic performance. *ACS Appl. Mater. Interfaces* 2012, **4**(9)**:** 4800-4806.

94. Zhang S, Xu W, Zeng M, Li J, Xu J, Wang X. Hierarchically grown CdS/alpha-Fe2O3 heterojunction nanocomposites with enhanced visible-light-driven photocatalytic performance. *Dalton Trans.* 2013, **42**(37)**:** 13417-13424.

95. Wang P, Wu H, Tang Y, Amal R, Ng YH. Electrodeposited Cu2O as Photoelectrodes with Controllable Conductivity Type for Solar Energy Conversion. *J. Phys. Chem. C* 2015, **119**(47)**:** 26275-26282.

96. Schreier M, Luo J, Gao P, Moehl T, Mayer MT, Gratzel M. Covalent Immobilization of a Molecular Catalyst on Cu2O Photocathodes for CO2 Reduction. *J. Am. Chem. Soc.* 2016, **138**(6)**:** 1938-1946.

97. Hou J, Yang C, Cheng H, Jiao S, Takeda O, Zhu H. High-performance

p-Cu2O/n-TaON heterojunction nanorod photoanodes passivated with an ultrathin carbon sheath for photoelectrochemical water splitting. *Energy Environ. Sci.* 2014, **7**(11)**:** 3758-3768.

98. Cheng C, Karuturi SK, Liu L, Liu J, Li H, Su LT*, et al.* Quantum-dot-sensitized TiO2 inverse opals for photoelectrochemical hydrogen generation. *Small* 2012, **8**(1)**:** 37-42.

99. Vasquez RP. Cu2O by XPS. *Surf. Sci. Spectra* 1998, **5**(4)**:** 257.

100. Liu Y, Zhou L, Hu Y, Guo C, Qian H, Zhang F*, et al.* Magnetic-field induced formation of 1D Fe3O4/C/CdS coaxial nanochains as highly efficient and reusable photocatalysts for water treatment. *J. Mater. Chem.* 2011, **21**(45)**:** 18359.

101. Rezk AR, Walia S, Ramanathan R, Nili H, Ou JZ, Bansal V*, et al.* Acoustic-Excitonic Coupling for Dynamic Photoluminescence Manipulation of Quasi-2D MoS2Nanoflakes. *Adv. Opt. Mater.* 2015, **3**(7)**:** 888-894.

102. Panzner G, Egert B, Schmidt HP. The stability of CuO and Cu2O surfaces during argon sputtering studied by XPS and AES. *Surf. Sci.* 1985, **151**(2-3)**:** 400-408.

103. Barreca D, Gasparotto A, Tondello E. CVD Cu2O and CuO Nanosystems Characterized by XPS. *Surf. Sci. Spectra* 2007, **14**(1)**:** 41.

104. Ai G, Li H, Liu S, Mo R, Zhong J. Solar Water Splitting by TiO2/CdS/Co-Pi Nanowire Array Photoanode Enhanced with Co-Pi as Hole Transfer Relay and CdS as Light Absorber. *Adv. Funct. Mater.* 2015, **25**(35)**:** 5706-5713.

105. Wang JC, Zhang L, Fang WX, Ren J, Li YY, Yao HC*, et al.* Enhanced Photoreduction CO(2) Activity over Direct Z-Scheme alpha-Fe(2)O(3)/Cu(2)O Heterostructures under Visible Light Irradiation. *ACS Appl. Mater. Interfaces* 2015, **7**(16)**:** 8631-8639.

106. Wang G, Ling Y, Wheeler DA, George KE, Horsley K, Heske C*, et al.* Facile synthesis of highly photoactive alpha-Fe(2)O(3)-based films for water oxidation. *Nano lett.* 2011, **11**(8)**:** 3503-3509.

107. Fan L, Long J, Gu Q, Huang H, Lin H, Wang X. Single-site nickel-grafted anatase TiO2 for hydrogen production: Toward understanding the nature of visible-light photocatalysis. *J. Catal.* 2014, **320:** 147-159.

108. Zhang GA, Cheng YF. Micro-electrochemical characterization and Mott–Schottky analysis of corrosion of welded X70 pipeline steel in carbonate/bicarbonate solution. *Electrochim. Acta* 2009, **55**(1)**:** 316-324.

109. Kennedy JH. Flatband Potentials and Donor Densities of Polycrystalline α-Fe[sub

2]O[sub 3] Determined from Mott-Schottky Plots. *J. Electrochem. Soc.* 1978, **125**(5)**:** 723.

110. De Gryse R. On the Interpretation of Mott-Schottky Plots Determined at Semiconductor/Electrolyte Systems. *J. Electrochem. Soc.* 1975, **122**(5)**:** 711.

111. Klahr B, Gimenez S, Fabregat-Santiago F, Hamann T, Bisquert J. Water oxidation at hematite photoelectrodes: the role of surface states. *J. Am. Chem. Soc.* 2012, **134**(9)**:** 4294-4302.

112. Smith RD, Prevot MS, Fagan RD, Zhang Z, Sedach PA, Siu MK*, et al.* Photochemical route for accessing amorphous metal oxide materials for water oxidation catalysis. *Science* 2013, **340**(6128)**:** 60-63.

113. Zhong DK, Cornuz M, Sivula K, Grätzel M, Gamelin DR. Photo-assisted electrodeposition of cobalt–phosphate (Co–Pi) catalyst on hematite photoanodes for solar water oxidation. *Energy Environ. Sci.* 2011, **4**(5)**:** 1759.

114. Jiao F, Frei H. Nanostructured cobalt oxide clusters in mesoporous silica as efficient oxygen-evolving catalysts. *Angew. Chem. Int. Ed.* 2009, **48**(10)**:** 1841-1844.

115. Xiang Q, Chen G, Lau T-C. Effects of morphology and exposed facets of α-Fe2O3nanocrystals on photocatalytic water oxidation. *RSC Adv.* 2015, **5**(64)**:** 52210-52216.

116. Chen X, Liu L, Yu PY, Mao SS. Increasing solar absorption for photocatalysis with black hydrogenated titanium dioxide nanocrystals. *Science* 2011, **331**(6018)**:** 746-750.

117. Steinmiller EM, Choi KS. Photochemical deposition of cobalt-based oxygen evolving catalyst on a semiconductor photoanode for solar oxygen production. *Proc. Natl. Acad. Sci. U. S. A.* 2009, **106**(49)**:** 20633-20636.

118. Ernst B, Bensaddik A, Hilaire L, Chaumette P, Kiennemann A. Study on a cobalt silica catalyst during reduction and Fischer–Tropsch reaction: In situ EXAFS compared to XPS and XRD. *Catal. Today* 1998, **39**(4)**:** 329-341.

119. Zhong DK, Gamelin DR. Photoelectrochemical water oxidation by cobalt catalyst ("Co-Pi")/alpha-Fe(2)O(3) composite photoanodes: oxygen evolution and resolution of a kinetic bottleneck. *J. Am. Chem. Soc.* 2010, **132**(12)**:** 4202-4207.

120. Long M, Cai W, Cai J, Zhou B, Chai X, Wu Y. Efficient photocatalytic degradation of phenol over Co3O4/BiVO4 composite under visible light irradiation. *J. Phys. Chem. B* 2006, **110**(41)**:** 20211-20216.

121. Long, Cai, Kisch H. Visible Light Induced Photoelectrochemical Properties of n-BiVO4and n-BiVO4/p-Co3O4. *J. Phys. Chem. C* 2008, **112**(2)**:** 548-554.

122. Sivula K. Metal Oxide Photoelectrodes for Solar Fuel Production, Surface Traps, and Catalysis. *J. Phys. Chem. Lett.* 2013, **4**(10)**:** 1624-1633.